# 2+1 correlation between $\pi^0$ and charged hadrons in Au-Au collisions at $\sqrt{s_{NN}}$=200GeV

by

**Yanyi He**

A thesis submitted to the graduate faculty

in partial fulfillment of the requirements for the degree of

MASTER OF SCIENCE

Major: Physics

Program of Study Committee:
Craig Ogilvie, Major Professor
Marzia Rosati
Joerg Schmalian
Kenneth J. Koehler

Iowa State University

Ames, Iowa

2009

Copyright © Yanyi He, 2009. All rights reserved.

# DEDICATION

I would like to dedicate this thesis to my family and my friends, without whose support I would not have been able to complete this work. I would also like to thank my advisor and experimental nuclear physics' senior graduate students for their guidance during the writing of this work.

# TABLE OF CONTENTS

LIST OF FIGURES----------vii

LIST OF TABLES----------x

ABSTRACT----------xi

CHAPTER 1. INTRODUCTION----------1

1.1 Quark Gluon Plasma and RHIC----------1

1.2 Comparison Systems: d-Au and p-p collision----------3

1.3 Kinetic Quantities Description of Au-Au Collision----------3

1.4 Elliptic Flow----------4

1.5 Hard Probe and Suppression----------6

1.6 Jet Model and Jet Correlation----------7

1.7 Definition of Correlation----------9

1.8 “2+1” Correlation----------12

1.9 Thesis Organization----------14

CHAPTER 2. PHENIX OVERVIEW----------15

2.1 PHENIX Overview----------15

2.2 Event Selection and Charaterization----------18

2.2.1 Beam Beam Counter----------18

2.2.2 Zero-Degree Calorimeters----------19

2.2.3 Centrality Measurement----------20

2.2.4 Minimum Bias Trigger----------21

2.3 Central Arms Detectors and Single Particle Measurement----------22

2.3.1 Central Arm Magnet----------22

2.3.2 Drift Chamber----------23

2.3.3 Pad Chambers----------26

2.3.4 Electro-Magnetic Calorimeter----------27

2.3.5 Ring Imaging Cherenkov Detector----------28

CHAPTER 3. DATA ANALYSIS----------29

3.1 Run & Event Selection----------30

3.2 Single Particle Selection----------32

3.2.1 Charged Particle Selection----------33

3.2.1.1 Track Quality Cut----------33

3.2.1.2 Drift Chamber Zed Cut----------36

3.2.1.3 Matching at PC3----------39

3.2.1.4 m2emc cut----------40

3.2.1.5 EP Cut in EMCal----------43

3.2.2 $\pi^0$ Selection & Photon Selection----------47

3.2.2.1 Photon Selection----------47

3.2.2.2 $\pi^0$ Selection----------50

CHAPTER 4. CORRELATION FUNCTION AND ZYAM METHOD----------55

4.1 Construction of Correlation Function----------55

4.1.1 Event Mixing----------56

4.1.2 Normalization----------57

4.1.3 $\upsilon_2$----------57

4.2 ZYAM ----------60

CHAPTER 5. Au-Au CORRELATION FUNCTION & CONCLUSION----------61

REFERENCES----------63

# LIST OF FIGURS


- **Fig 1.1** QCD energy density as a function of temperature
- **Fig.1. 2** Schematic diagram of non-head on nuclear collision. The overlap (shaded grey) almond shaped region is the place of participating nucleons. The reaction plane is defined as the short length of overlap region
- **Fig.1.3** Comparison of ratio of single particle spectra in d-Au collisions(open and closed circles) and Au-Au collisions (triangles) compared to binary-scaled p-p collisions
- **Fig.1.4** A typical plot of correlation functions. Each panel is from a different centrality Au-Au collision, while the same p+p correlation is in all panels as reference.
- **Fig.1.5** Per-trigger yield versus $\Delta\phi$ for various trigger and partner $p_T$s, in p + p and 0-20% Au+Au collisions. The Data in some panels are scaled. Solid lines (shaded bands) are the elliptic flow (ZYAM).
- **Fig.1.6** A schematic drawing of "2+1" correlation. On the left side, the existing of "conditional" particle shifts the hard scattering to center of medium, and both partons survive the medium and produce high-$p_T$ particles. On the right side, it shows the possibility that a normal 2-particle correlation has its away–side parton absorbed in the medium and no high-$p_T$ particle created on the away side.
- **Fig. 2.1** Run7 layout of PHENIX Detector
- **Fig.2.2** Fractional ZDC energy distribution as a function of fractional BBC charge distribution for minimum bias Au-Au collisions.
- **Fig.2.3** Magnetic Field Lines Distribution with outer Central Magnet Coil Energized.

- **Fig. 2.4** Side view of a drift chamber sector showing the positions of the wire layers. Also shown is the wire positions for the V1 layer (other layers are similar).
- **Fig 2.5** A drawing of tracking parameters for the drift chamber. $\alpha$ is the track's deflection from a straight line and $\phi$ is the azimuthal angle of the track measured at the drift chamber reference radius of 220cm.
- **Fig 2.6** 3D view of PCs.
- **Fig. 3.1** A run-group threshold plot, run numbers verse run-mean-$p_T$ distribution, generated by the calibrators database.
- **Fig.3.2** A typical "bad" run is shown here. Centrality distribution is obviously deviated from a flat line
- **Fig .3.3** The plot of Quality. Qual==31 and qual==63 are dominated.
- **Fig. 3.4** Single quality cut effect plot. The left panel is the plot of ratio of number of events removed by 2 sigma square cut on PC3 over 1 sigma square cut. The right panel is the spectrum of charged hadrons. The red line is after applying the quality cut (pqual>=31), the black line is without any cut for comparison.
- **Fig.3.5** Z position in DC with cut |zed|<75 cm. It's almost flat in both positive and negative region which corresponds to the randomness of hitting in DC.
- **Fig.3.6** Single zed cut effect plot. The left panel is the plot of ratio of number of events removed by 2 sigma square cut on PC3 over 1 sigma square cut. The right panel is the spectrum of charged hadrons. The red line is after applying the zed cut (|zed$\pm$20|<40 cm), the black line is without any cut for comparison.

- **Fig.3.7** An example plot of PC3 matching distribution of DC/PC1 tracks in $\phi$ direction
- **Fig.3.8** a typical plot of $m^2$ distribution in EMCal. The first peak is for photon, nearly peak at zero. The second peak is for kaon, there is another subtle peak at around 1 is for proton.
- **Fig. 3.9** Single m2emc cut effect plot. The left panel is the plot of ratio of number of events removed by 2 sigma square cut on PC3 over 1 sigma square cut. The right panel is the spectrum of charged hadrons. The red line is after applying the m2emc cut (-0.5<m2emc<1.5Gev), the black line is without any cut for comparison.
- **Fig.3.10** EP distribution. Red line is e-0.3-0.15*p=0. E is y axis and p is momentum as X axis.
- **Fig.3.11** Single ep cut effect plot. The left panel is the plot of ratio of number of events removed by 2 sigma circular cut on PC3 over 1 sigma circular cut. The right panel is the spectrum of charged hadrons. The red line is after applying the ep cut(e-0.3-0.15*p), the black line is without any cut for comparison.
- **Fig.3.12** Single prob cut effect plot. The left panel is the plot of ratio of number of events removed by 2 sigma square cut on PC3 over 1 sigma square cut. The right panel is the spectrum of charged hadrons. The red line is after applying the probability cut (lprob>0.2), the black line is without any cut for comparison.
- **Fig.3.13** 2-dimension plot of PC3 in $\phi$ and z. The red shape represents for the fitting function. With good trigger cut, ($\pi^0$ selection )and m2emc cut, ep cut, ratio of S/(S+B) with $dz^2 + d\phi^2$<4 is 99.14%.

- **Fig. 3.14** An example plot of EMCal $\chi^2$ distribution
- **Fig .3.15** a typical tower map for one sector in EMC, Each tiny squares in the plot represent one EMCal tower.
- **Fig.3. 15** pi0 invariant mass with starting cuts (asymmetry<0.8, lpt>5 GeV). The S/B ratio is 0.2.
- **Fig.3.16** Pi0 invariant mass additionally with asymmetry cut: asymmetry< 0.4+0.004*centc. The S/B ratio is 0.6.
- **Fig. 3.17** plot of $\pi^0$ invariant mass with all promising cuts. The area under blue line is for the fitting background, the area between the red line and blue line is for the signal.
- **Fig.4.1** Raw Pair distribution of real events. It peaks at $\Delta\phi = 0$ or $\pi$.
- **Fig.4.2** The published PHENIX measurement of $v_2$ in Au-Au and Cu-Cu as a function of centrality and $p_T$
- **Fig.4.3** Comparing correlation functions of Cu-Cu (top) to p-p (bottom). Acceptance effects already corrected. Flow background from ZYAM method is marked on Cu-Cu plots.
- **Fig.5.1** Draft correlation function. The red line is straight line showing y=0 baseline.

# LIST OF TABLES


- **Tab. 2.1** Summary of the PHENIX Detector Subsystems [16]
- **Tab. 3.1** Effectiveness comparison between different cuts

# ABSTRACT

In Au-Au collision at $\sqrt{s_{NN}}$=200 GeV, a transition to Quark-Gluon Plasma can happened. High-momentum parton lose energy when travel through the hot dense matter, fragment into jets. If we can study the correlation between trigger particle $\pi^0$ and charged hadrons in the jets, it is helpful to understand the energy loss mechanism and hence some properties of Quark-Gluon Plasma. My work is to select the qualified and robust trigger particles and charged hadrons for correlation function.

# CHAPTER 1. INTRODUCTION

## 1.1 Quark Gluon Plasma and RHIC

Relativistic Heavy Ion Collider (RHIC) at Brookhaven National Laboratory, New York is to study Quantum Chromodynamic (QCD) matter under extreme temperatures and densities by mimic a phase of matter not seen since a few micro-seconds after the Big Bang. Under this extreme conditions, the universe's temperature was so high that quarks and gluons were not bound inside the size of nucleons (~1fm, protons and neutrons), but existed as a quark-gluon plasma (QGP). As the universe cooled, quarks and gluons became confined in nucleons by the strong force. As the universe cooled further, atomic matter, which dominates the visible universe, today formed. Most plots in this chapter are from PHENIX white paper[1].

Fig. 1.1 is the plot of energy density as a function of temperature where a large increase in the energy density is calculated at the critical temperature. This critical temperature is approximately 170 MeV or, in more familiar units, about $10^{12}$K. Fig. 1.1 shows that even at 4 times the critical temperature, the energy density is still below the Stefan-Boltzmann limit for a dilute gas (non-interacting particles). Since the limit is not reached even at 4 times the critical temperature, which means the matter is interacting to some extent. Theoretical evidence for the existence of the phase transition is based on lattice QCD. The results of the lattice calculations show that the energy density required for a phase transition to a QGP is 1 GeV/fm$^3$. This energy density in collision region can be estimated by experiments using the Bjorken energy density [Bjorken, 1983][2]. This leads to an energy

density of 15 GeV/fm$^3$ in Au-Au collision at 200GeV [3], which is significantly larger than the requirement of phase transition.

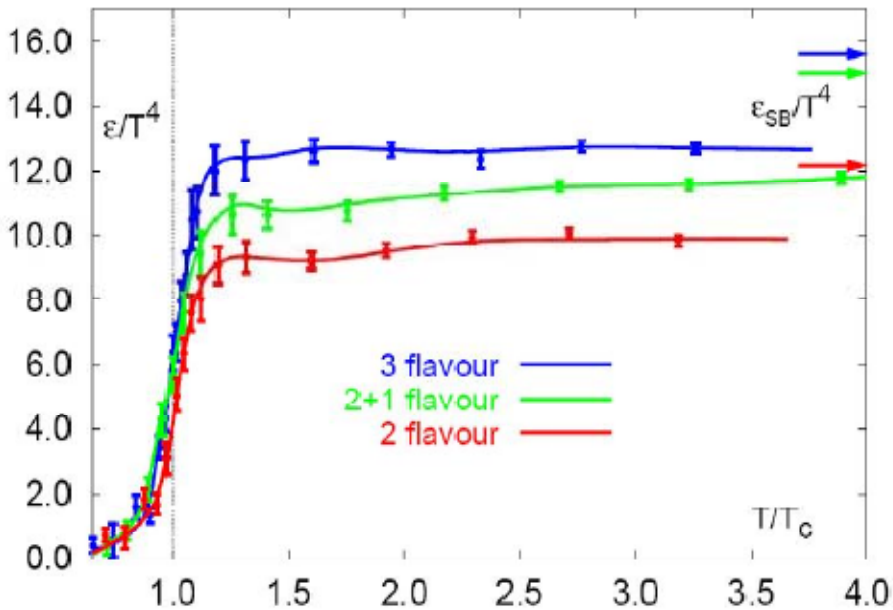


Fig 1.1 QCD energy density as a function of temperature

However, the QGP created in the collision only has a life time on the order of 10fm/C, too short to be measured. Most particles leave the collision region at nearly the speed of light, the size of the collision system is on the order of $10^{-14}$m. The Properties of the systems can only be studied indirectly from the remnants of the collision which will pass through and are detected by detectors a few meters away from the collision region. Particles of interest are the remains of inelastic parton and nucleon scattering during the collision. The non-interaction pieces of the Au nuclei continue forward in the beam direction after the collision. Properties of the medium can be measured from the interactions between the particles as they leave the interaction region. The collisions data used in this thesis were measured by the PHENIX detector.

## 1.2 Comparison Systems: d-Au and p-p collisions

Au has 79 protons and 118 neutrons and doesn't have any other natural isotopes. Due to the large number of protons and neutrons in Au, Au-Au collision can create a few thousand particles in a head-on collision at high energy. It is necessary to compare the measurements with simpler systems. p-p collision and d-Au collision at the same energy per nucleon are measured at RHIC as the comparison or control systems. Although these two types of collisions do not create the hot dense matter made in Au-Au collision, we can still find many other similar properties in right before and after collision times. Formation processes for the final observed hadrons should be similar in all three collision systems. d-Au collisions provide additional information about nuclear effects due to the initial state of the large nuclei. Because the charge to mass ratio is closer to gold for deuterons than for proton, deuterons are used. Besides, no significant nuclear effects are expected from the addition of a single neutron. With this control system, we can easily determine the changes in the final state of Au-Au collision come from the hot dense medium or condition in the initial nuclei.

## 1.3 Kinetic Quantities Descriptions of Au-Au Collision

- ***Center of Mass Energy***: The collision energy per nucleon pair is $\sqrt{s_{NN}}$, The collisions studied in my thesis all have $\sqrt{s_{NN}}$=200GeV, what is to say each beam momentum is 100GeV/nucleon
- ***Transverse Momentum***: in the analysis, particles are classified by their transverse momentum-$p_T$, the projection of momentum onto the plane perpendicular to the beam axis.

- ***Rapidity***: y, is related to the particle's total energy and momentum along the beam axis.

$$y = \frac{1}{2}\log\frac{E+p_z}{E-p_z} \quad (1.1)$$

- ***Pseudo-rapidity***: very useful to measure the particle's angle θ with respect to the beam axis.

$$\eta = \frac{1}{2}\log\ \tan\frac{\theta}{2} \quad (1.2)$$

- ***Centrality***: measurement of overlapping area of two colliding nuclei. Any parameters that can describe the overlapping area with a monotonic function can be used for centrality. Three commonly used parameters related to the collision centrality are impact parameter, the number of binary collisions, $N_{coll}$, and the number of participating nucleons, $N_{part}$. Further discussion is in next chapter.
- ***Fragmentation***: A process of outgoing scattered parton radiates gluons which split into quark and anti-quark pairs. These pairs turn into observed jets of hadrons.

## 1.4 Elliptic Flow

Due to the almond shaped nuclear overlap region in Figure 1.2 in peripheral collisions, the pressure gradient is larger in the shorter direction of the ellipsoid. This produces an observable asymmetric momentum distribution-elliptic flow. Pressure gradient with respect to the short axis in the reaction plane correlates particles with the reaction plane. The single particle distribution can be written as a Fourier transform where the 2nd Fourier coefficient is the leading term, any higher order coefficients are ignored since they are much smaller than $\nu_2$, $\nu_1$ is zero due to the symmetry of the elliptic flow.

$$\frac{dN}{d\phi dp_T} = \frac{N}{2\pi}(1 + \nu_2(p_T)\cos(2\phi)) \quad (1.3)$$

The coefficient $\nu_2$ is a parameter of the strength of the correlation and very sensitive to the pressure gradients in the overlap region. The $\nu_2$ measured at RHIC are larger than expected, which is expected to exist large pressure gradients and strong collective motion of the elements of the medium.

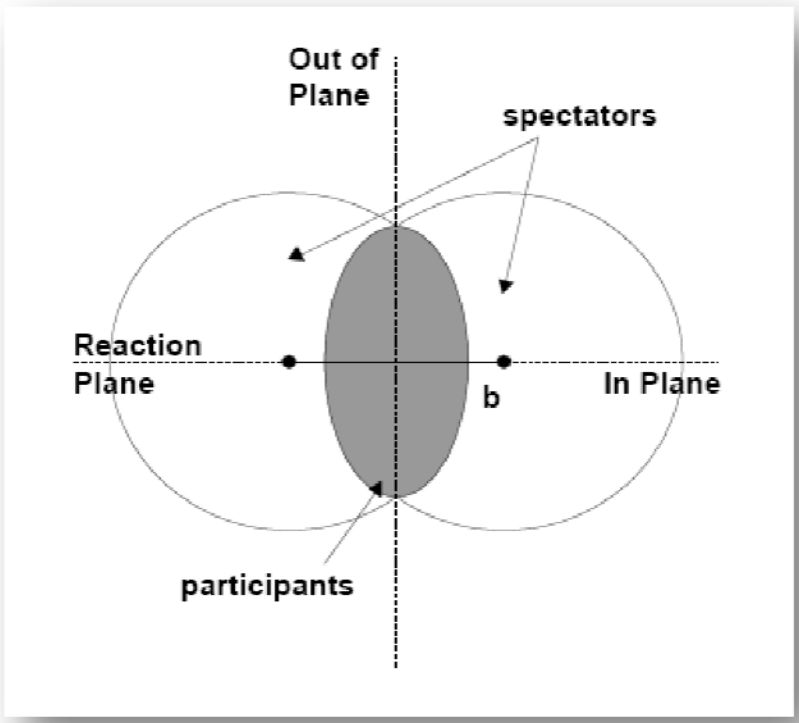


Fig1.2 Schematic diagram of non-head on nuclear collision. The overlap (shaded grey) almond shaped region is the place of participating nucleons. The reaction plane is defined as the short length of overlap region

## 1.5 Hard Probe and Suppression

When two Au nuclei collides, hard scattering takes places as QGP is being formed in soft scattering. Hard scattered partons travel through plasma, scatter with medium, then lose energy. The energy loss might be from radiate gluons. Parton now has lower energy, and fragments into bound hadrons in restricted angle, collectively jets. Hardons in jets are lower in $p_T$, which we can observe by comparing inclusive production in Au-Au collisions with p-p collisions by forming the ratio

$$R_{AA} = \frac{\frac{1}{2\pi p_T N_{evt}} \frac{dN_{Au+Au}}{dp_T dy}}{<N_{coll}> \frac{1}{2\pi p_T N_{evt}} \frac{dN_{p+p}}{dp_T dy}} \quad (1.4)$$

Where *<Ncoll>* is the average number of nucleon-nucleon (binary) collisions in the overlap region of the Au-Au collision.

The interpretation of $R_{AA}$is if $R_{AA}$ = 1, then the Au-Au production is an incoherent superposition of p-p collisions, no nuclear effects. Obviously, from Fig. 1.3 in central Au-Au collisions there is a suppression compared to binary-scaled p-p collisions. The suppression is not present in d-Au collisions, the strong suppression in Au-Au collision is an effect that is unique to the Au-Au collisions. Suppression is explained as a result of partons losing energy while traveling in the hot dense medium created in Au-Au collisions. Since partons lose their energy, the average momentum of the fragmentation high-$p_T$ hadrons are also reduced respectively, relative to those in the vacuum, such as in p-p collisions.

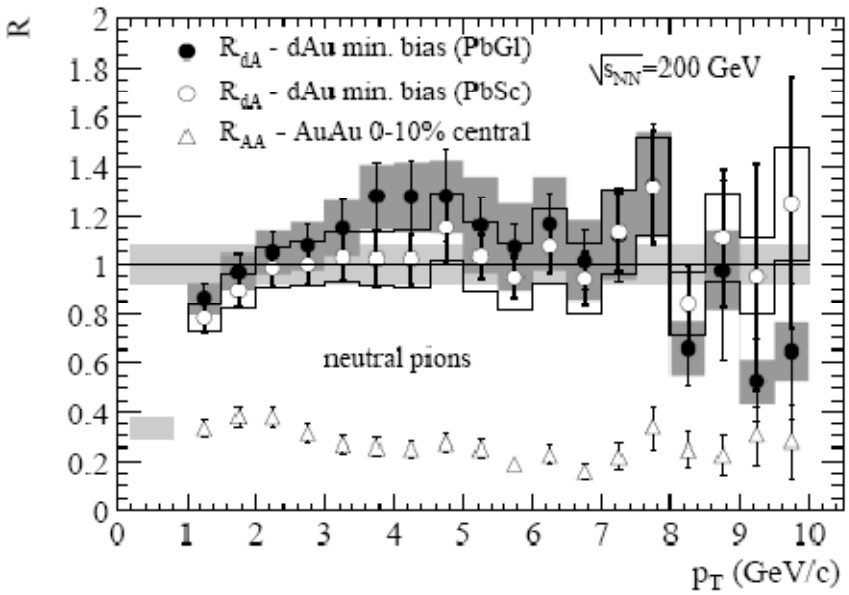


Fig.1.3 Comparison of ratio of single particle spectra in d-Au collisions(open and closed circles) and Au-Au collisions (triangles) compared to binary-scaled p-p collisions

## 1.6 Jet Model and Jet Correlation

A hard-scattered parton in vacuum fragments into multiple particles within a restricted angular region, known as a jet. The jets' multiplicity and width characteristics provide information for the fragmentation process of partons into hadrons. Quantitative method of event-by-event jet finding is generally done by either cone jet finders, where a large amount of energy inside a cone of half angle $R = \sqrt{\Delta\phi^2 + \Delta\eta^2}$ is defined as a jet. R is 0.7, or $k_\perp$ jet finder [4] combines particles with small emission angles.

However, in the Au-Au collision there lies in a large soft background, which makes it hard to reconstruct a full event-by-event jet. PHENIX applied a statistical method to study jets, called 2-particle azimuthal-angle correlations.

Fig1.4 below is a typical plot of correlation function. In this figure, the jet signals are a function of the relative azimuthal angle Δϕ between pairs of particles in Au-Au collisions in different centrality regions, 0-20%,20-40%,60-92% after subtracting combinatoric background. The p-p data are also draw in the plot as a reference. In each panel, at the region of |Δϕ | ~ 0 the jet peak is clearly visible, and the region of |Δϕ | ~ π indicate the back-to-back jet if any. The definition and a more clear explanation of correlation function are in next section.

We don't see a strong suppression at the region of |Δϕ | ~ 0, however if we compare the most central Au-Au jet signals in Fig1.4, there do be an observable strong suppression of jets at the region of |Δϕ | ~ π. This is because hard scattering processes produce a pair of back-to-back jets and the hadrons spectrum within the jets will be modified if the parton fragments after losing energy while passing through dense matter [5].

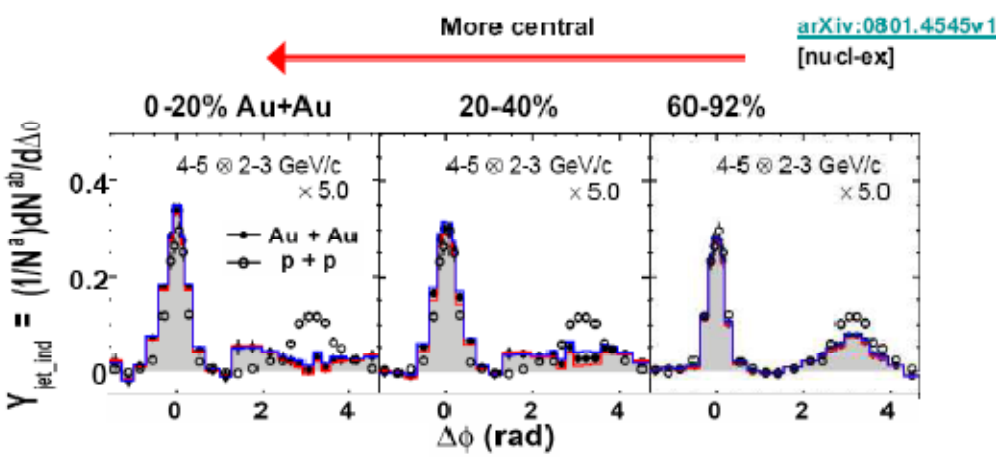


Fig1.4 A typical plot of correlation functions. Each panel is from a different centrality Au+Au collision, while the same p+p correlation is in all panels as reference.

To quantify the suppression of jets, theorists have predicted the angular distribution and number of jet fragments by calculating the coupling of jets to a strongly interacting medium [8,9,10,11,12,13,14,15].

## 1.7 Definition of Correlation

In the center-of-mass reference frame, the fragmentation products from a jet are tightly correlated in $\phi$ and in $\eta$ space. If two particles fragment from the same jet, their momentum vectors will have tight correlation at the region of close in $\phi$, $|\Delta\phi|\sim 0$and in $\eta$; if the hadrons fragment from two back-to-back parton jets, they will have a high probability of being back-to-back or $|\Delta\phi|\sim \pi$. Since $\eta$ coverage is much less than $\phi$ coverage, correlation function in our analysis will focus on the azimuthal space.

Jets are traditionally reconstructed by tagging a high-energy leading or trigger particle, then count the relative low-energy particles around. In a full-coverage and low soft background experiment, the event-by-event jet reconstruction is doable. This method is very successful in low multiplicity e+ - e− collisions. In higher-energy p-p collisions this method works too if the jet energies are very high and the detector has very good acceptance coverage.

However, neither condition above is well met in PHENIX, even if both jets fly within the PHENIX central-arm acceptance. In Au-Au collision, due to large number of interacting nucleons, the soft underlying background is very large even at region of $p_T >$ 2GeV/C. Besides, the PHENIX detector has roughly one third of full coverage, thus an average multiplicity of 10 particles for a given p-p event is incident on PHENIX. Considering the actual detector efficiency, this is a multiplicity too low for event-by-event jet

reconstruction. Instead, we will apply a technique of statistical measurement, two-particle correlations.

If two particles produced in a given event, one at $\phi_A, \eta_A$, and one at $\phi_B, \eta_B$, the correlation between the two particles is written as

$$C(\Delta\phi, \Delta\eta) = \frac{\mathrm{Prob}(\phi_A, \eta_A, \phi_B, \eta_B)}{\mathrm{Prob}(\phi_A, \eta_A)\mathrm{Prob}(\phi_B, \eta_B)} \quad (1.5)$$

$\mathrm{Prob}(\phi_A, \eta_A, \phi_B, \eta_B)$ is the probability of finding 2 particles in an event, $\mathrm{Prob}(\phi_A, \eta_A)$ and $\mathrm{Prob}(\phi_B, \eta_B)$ are probability of finding a single particle. $\Delta\phi = \phi_A - \phi_B, \Delta\eta = \eta_A - \eta_B$ is the relative azimuth and pseudo-rapidity of two particles.

In sum, to study the travelling parton's energy-loss mechanisms, the PHENIX experiment at RHIC measures azimuthally 2-particle jet correlations, within a different range of centrality in Au-Au collisions and transverse momentum of hadrons. Different categories of particles are also used to specifically measure certain energy-loss mechanisms.

In the recent PHENIX publications , measurements (shown in Fig.1.5 as an example) establish that the angular widths of the same-side jet correlations are at the same level (if not narrower) within errors comparing central Au-Au collisions to p-p collisions. Since this Gaussian width is a unique characteristic of the parton fragmentation process, it's reasonable to think that high $p_T$ trigger hadrons in Au-Au collision are mainly from hard scattering followed by jet fragmentation, as those in p-p collision.

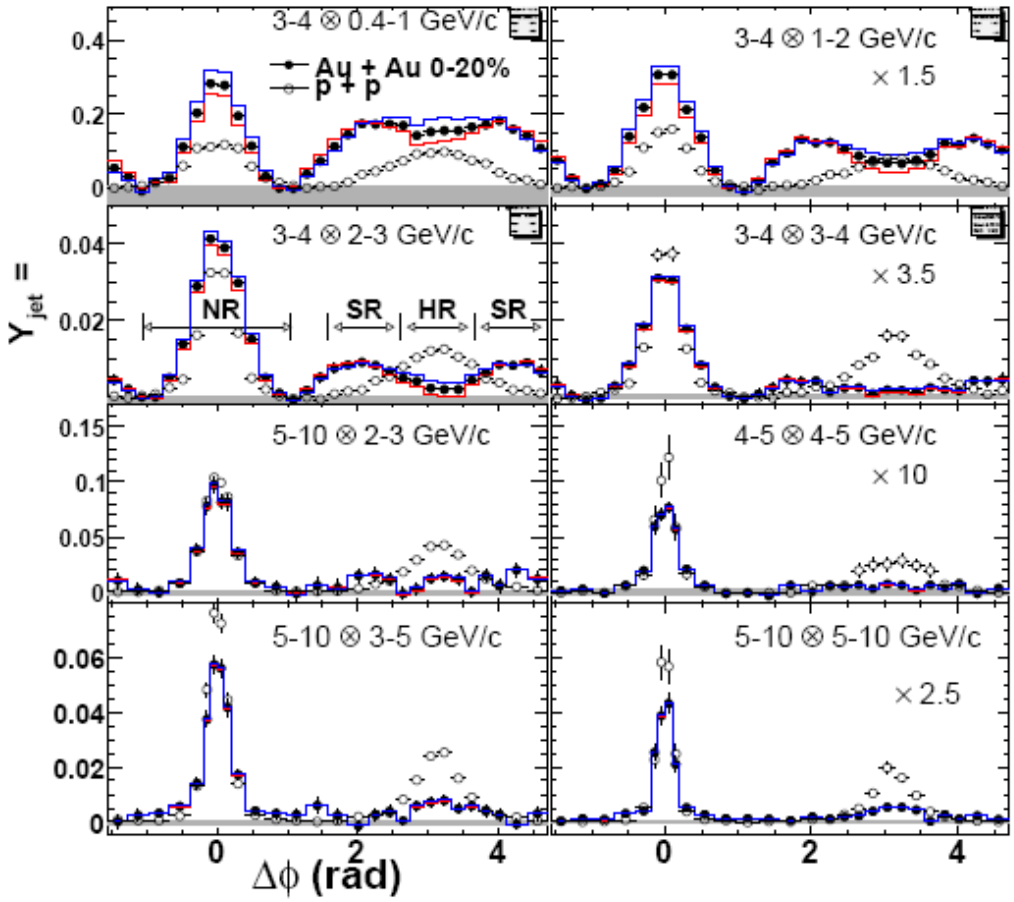


Fig1.5 Per-trigger yield versus Δϕ for various trigger and partner $p_T$s, in p + p and 0-20% Au+Au collisions. The Data in some panels are scaled. Solid lines (shaded bands) is the elliptic flow (ZYAM).

This figure [6] also shows clear evidence of medium modifications of the fragmentation multiplicity, as well as the yield suppression of the far-side jet in Au-Au collisions. The key conclusion from this suppression in that the parton that fragments into far-side hadrons loses energy before it fragments. This suppression depends on many factors, such as re-combination of fragmentation products and the medium to produce additional hadrons, and surface-bias: the likelihood that the high-$p_T$ trigger hadron is more likely to be

detected if the hard-scattering takes place near the surface of the dense medium. Surface-bias is not easily observable in single high-$p_T$ probes spectrum measurement.

## 1.8 "2+1" Correlation

As we discussed before, there exists clear evidence of medium effect in Au-Au collision at RHIC that high-momentum parton will lose energy when they travel through the dense QGP and lead to a suppressions. However, the single inclusive high-$p_T$ spectra is not sufficient to exclude many theory models on energy-loss mechanism, and we can't exclude the possibility of those high-$p_T$ particles not produced directly from a hard scattering process. Thus, we need a new method which is more sensitive to the multiple theoretic models.

The two-particle correlation is powerful for Au-Au collision since it statistically removes the large soft underlying background. However, there is a surface-bias when we select on a high-$p_T$ trigger as the preferentially selects hard-scattering locations near the surface. The goal of the "2+1" correlation is to shift and control this surface bias. The goal of this thesis is to make sure the particles used in a "2+1" correlation analysis are robustly reconstructed with as low as possible contamination from fake tracks. Before reconstruction the events, we will use different cuts on the variable to reduce the contamination. The applied cuts and their effectiveness will be showed in following chapters.

Current theory models have their calculations based on parameters of the density and path-length of medium traveled by survival partons. The difficulty is those partons are predominantly from the surface of the dense matter which will result in surface bias.

One idea is doing the "2+1 correlation". We select a high-$p_T$ particle as trigger of the correlation, and a second high-$p_T$ back-to-back particle as the conditional particle.

Requiring the second conditional particles removes some of the hard-scattering events that take place near the surface. The back-to-back hadrons from these do not have enough energy to meet the $p_T$ requirement. Hence this shifts the distribution of hard-scattering locations to more within the hot, dense matter. Partons that travel a longer length in the medium before fragmenting into near-side hadrons are more of interest in the analysis work.

For both trigger and conditional particles to survive after their passage through the medium and produce high-$p_T$ hadrons, they must travel comparable path-lengths through the dense Quark Matter. The events excluded additionally by the "2+1" correlation are those that hard-scattering locations nearby the surface of medium. Fig.1.6 is a schematic drawing of "2+1" correlation. They are likely to have one jet traveling a short distance in the medium and presenting a high-$p_T$ trigger, but won't give the presence of the "conditional" high-$p_T$ hadron on the away-side because the back-to-back jet is most likely to be absorbed in the medium. These events would have been included in our "normal" 2-particle correlation analysis, because they do provide a high-$p_T$ trigger at near-side. Since we remove them, we shift the average location of hard scattering towards the center of the medium, statistically. By comparing the near-side jet shape of "2+1" correlation function to those usual 2−particle correlation function, we shall have a better understanding of how jets are affected by the medium and thus the properties of this hot-dense medium.

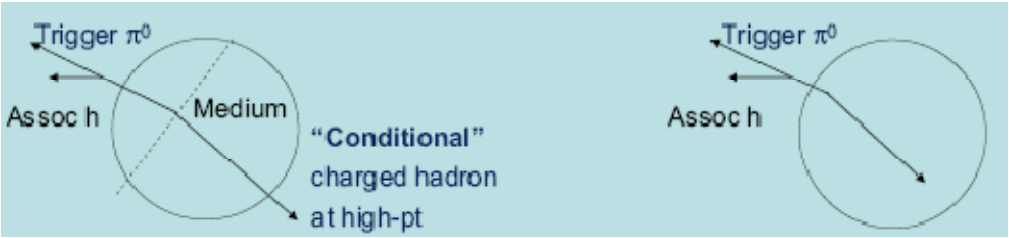


Fig 1.6 A schematic drawing of "2+1" correlation. On the left side, the existing of "conditional" particle shifts the hard scattering to center of medium, and both partons survive the medium and produce high-$p_T$ particles. On the right side, it shows the possibility that a normal 2-particle correlation has its away–side parton absorbed in the medium and no high-$p_T$ particle created on the away side.

## 1.9 Thesis Organization

In the following chapters, chapter 2 describes the PHENIX overview and its detectors. Particles' tracking algorithm reconstruction methodology will be introduced in chapter 3 and 4, my thesis is concentrated on how to remove backgrounds and selecting the most robust data for the correlation. The detailed algorithm of correlation function is in chapter 5, where also present the conclusion from my thesis work.

# CHAPTER 2. PHENIX OVERVIEW

## 2.1 PHENIX Overview

PHENIX (Pioneering High Energy Nuclear Interaction eXperiment) is a complex and multi-purpose detector system composed of 11 subsystems, which can carry out the measurement of hadrons and photons with excellent momentum and energy resolution. The object is to achieve high enough energy density to reach the phase change region in QCD.

The PHENIX subsystems are grouped into four spectrometer arms-two around mid-rapidity (the east and west central arms) and two at forward rapidity (the north and south muon arms), and a set of global detectors at high rapidity for measuring global event characteristics.

The central arms, each covering 90 degrees in azimuth, are centered around midrapidity $-0.35 < \eta < 0.35$, and are instrumented to detect electrons, photons, and charged hadrons in the mid-rapidity region. The muon arms, with $1.2 < \eta < 2.2$, have full azimuthal coverage and are instrumented to detect muons. The global detectors, Zero-Degree Calorimeters and Beam-Beam Counters, are placed close to the beam pipe. This set of detectors is used to determine global event information, including centrality as an observable of the time and the position of the interactions.

The run7 layout of PHENIX detector is shown in Fig. 2.1. The rapidity and azimuthal angle ($\Phi$) coverage, together with the physics abilities of each subsystems are listed in Table 2.1.

The PHENIX coordinate system is defined relative to the beam axis, which is z axis. The polar angle with respect to this axis is $\theta$. The azimuthal angle around the z axis is $\phi$ with $\phi = 0$ pointing into the West Arm. The origin is located at the center of two Beam-Beam

Counters along the beam axis. The *x* axis is pointing horizontally to the west arm. The *y* axis points upwards.

One central magnet and two muon magnets generate an axial magnetic field for the central arm and a radial field for the muon arms, respectively. The magnetic field bends the charged tracks and is used for momentum measurement.

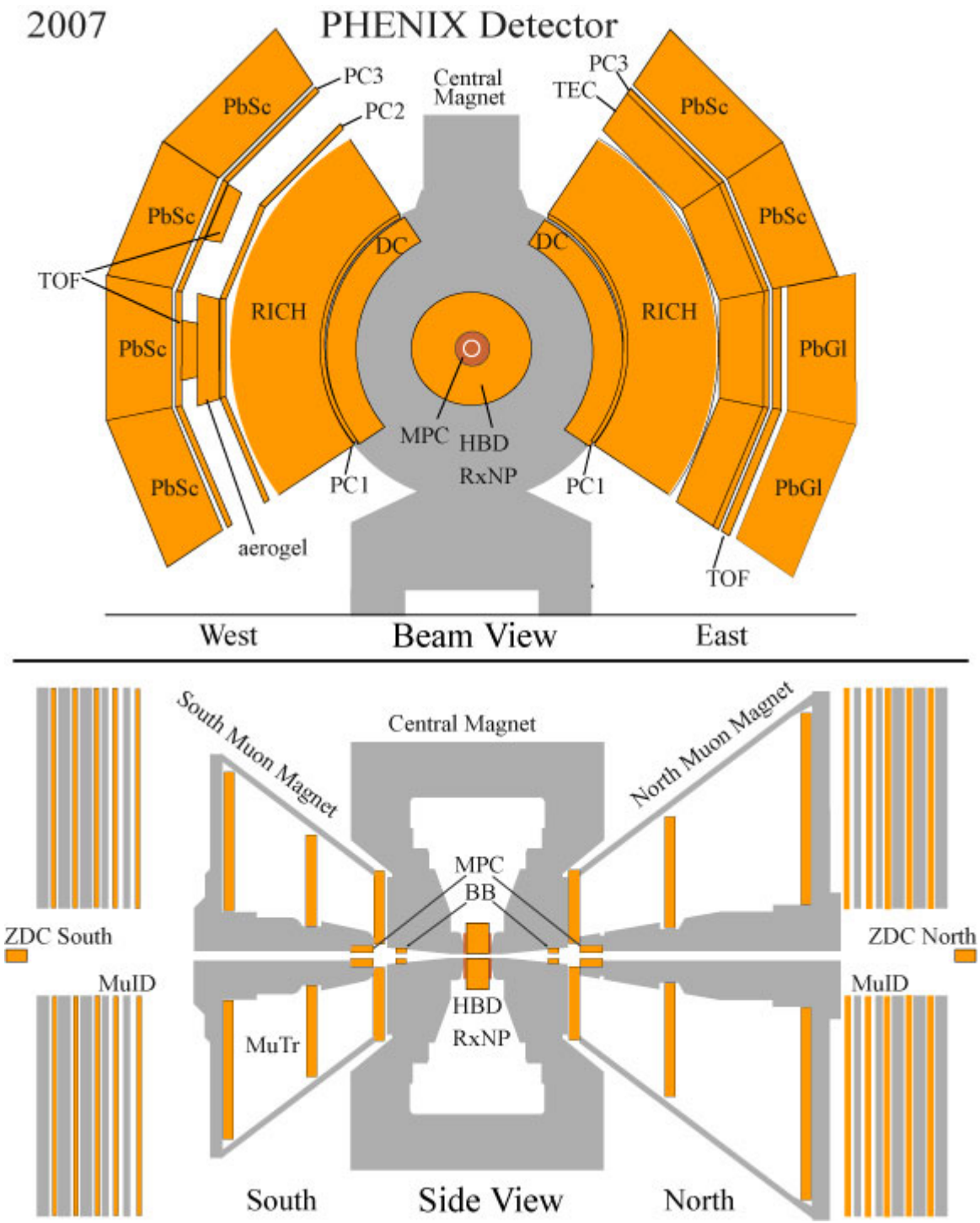

Fig. 2.1 Baseline layout of PHENIX Detector

Table 2.1 Summary of the PHENIX Detector Subsystems [16]

| Element | $\Delta\eta$ | $\Delta\phi$ | Purpose and Special Features |
|---|---|---|---|
| Magnet: central (CM) | $\pm 0.35$ | $360°$ | Up to 1.15 T·m. |
| muon (MMS) | -1.1 to -2.2 | $360°$ | 0.72 T·m for $\eta = 2$ |
| muon (MMN) | 1.1 to 2.4 | $360°$ | 0.72 T·m for $\eta = 2$ |
| Silicon (MVD) | $\pm 2.6$ | $360°$ | $d^2N/d\eta d\phi$, precise vertex, reaction plane determination |
| Beam-beam (BBC) | $\pm$(3.1 to 3.9) | $360°$ | Start timing, fast vertex. |
| NTC | $\pm$(1 to 2) | $320°$ | Extend coverage of BBC for p-p and p-A. |
| ZDC | $\pm 2$ mrad | $360°$ | Minimum bias trigger. |
| Drift chambers (DC) | $\pm 0.35$ | $90° \times 2$ | Good momentum and mass resolution, $\Delta m/m = 0.4\%$ at $m = 1$GeV. |
| Pad chambers (PC) | $\pm 0.35$ | $90° \times 2$ | Pattern recognition, tracking for nonbend direction. |
| TEC | $\pm 0.35$ | $90°$ | Pattern recognition, $dE/dx$. |
| RICH | $\pm 0.35$ | $90° \times 2$ | Electron identification. |
| ToF | $\pm 0.35$ | $45°$ | Good hadron identification, $\sigma$ <100 ps. |
| T0 | $\pm 0.35$ | $45°$ | Improve ToF timing for p-p and p-A. |
| PbSc EMCal | $\pm 0.35$ | $90°+45°$ | For both calorimeters, photon and electron detection. |
| PbGl EMCal | $\pm 0.35$ | $45°$ | Good $e^{\pm}/\pi^{\pm}$ separation at $p > 1$ GeV/c by EM shower and $p < 0.35$ GeV/c by ToF. $K^{\pm}/\pi^{\pm}$ separation up to 1 GeV/c by ToF. |
| $\mu$ tracker: ($\mu$TS) | -1.15 to -2.25 | $360°$ | Tracking for muons. |
| ($\mu$TN) | 1.15 to 2.44 | $360°$ | Muon tracker north installed for year-3 |
| $\mu$ identifier: ($\mu$IDS) | -1.15 to -2.25 | $360°$ | Steel absorbers and Iarocci tubes for |
| ($\mu$IDN) | 1.15 to 2.44 | $360°$ | muon/hadron separation. |

## 2.2 Event Selection and Charaterizations

### 2.2.1 Beam Beam Counter

PHENIX has two identical Beam-Beam Counters (BBCs) located at $3 < \eta < 3.9$ with $2\pi$ azimuthal coverage. Each BBC is an arrays of 64 quartz Cherenkov detectors, which measure relativistic charged particles produced in cones around each beam. BBCs are installed on the North and South sides of PHENIX and are located 1.44 m from the center of the interaction region directly behind the central magnet. The inner (outer) radius of the BBC is 5cm (30cm), having about 1cm space from the beam-pipe.

The BBCs are designed to measure the collision vertex position along the z axis, to trigger minimum bias events and to provide a start time for the PHENIX TOF system based on the average hit time in each BBC. More detailed information on the BBC's can be found in [17].

The start time ($T_0$) and the vertex position along the beam axis ($z_{vtx}$) are calculated as

$$T_0 = \frac{T_1+T_2}{2} \quad (2.1)$$

$$z_{vtx} = (T_1 - T_2)/2c \quad (2.2)$$

$T_1$ and $T_2$ are the average timing of particles in each counter and *c* is the speed of light.

### 2.2.2 Zero-Degree Calorimeters

The main role of Zero Degree Calorimeters (ZDC) is to provide the information of overlapping geometry in nuclei-nuclei collision, by measuring a clear portion of neutrons from the nuclei after collisions. The ZDCs are small hadronic calorimeters which can measure neutral energy. Charged particles are deflected out of the ZDC acceptance by the beam bending magnets leading to a measurement of neutron energy with very low background. This energy deposit comes from the part of nuclei, which did not participate in the collision and gives a direct measurement of colliding geometry. In PHENIX they are near the muon identification system along the beam pipe direction 18 m to the North and South of the collision region. The time difference between the neutron signals in the ZDC North and ZDC South can be used to determine the vertex position along the z. This is used when the BBC is not able to reconstruct the vertex. For further information on the ZDC's see Reference [18].

### 2.2.3 Centrality Measurement

Centrality is defined to describe the overlapping area of two colliding nuclei. This collision centrality can be quantized from any variable of a monotonic function of impact parameter, such as total multiplicity, total transverse energy, etc.

The centrality for PHENIX Au-Au collisions is calculated with a correlation of the charge measured by the BBC and the energy deposited in the ZDC. Signal in BBCs is proportional to the total number of collision participants-$N_{part}$, until the most central collisions where the BBC is saturated. The ZDC energy is proportional to the number of spectator neutrons, those neutrons from the Au nuclei uninvolved in the collision which continue forward in the beam direction. Figure 2.2 shows the normalized ZDC energy distribution as a function of the normalized BBC charge distribution. The solid lines mark the different centrality selections. Low centralities correspond to events with a small impact parameter.

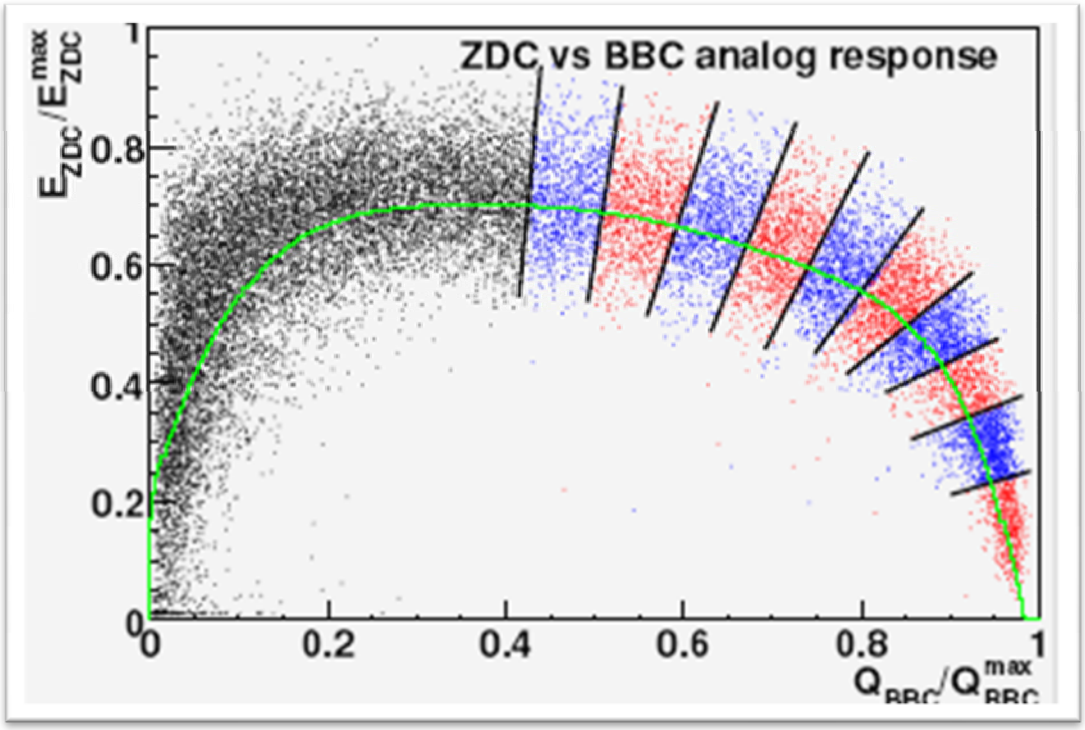


Fig2.2 Fractional ZDC energy distribution as a function of fractional BBC charge distribution for minimum bias Au-Au collisions.

### 2.2.4 Minimum bias Trigger

Because the computing ability for recording is limited and usually lower than the collision-event rate that happened in the interaction region, it's very crucial to filter events based on their detector response and give a higher priority to events of probably interesting physics. This mechanism is called "level-one trigger" In PHENIX. Minbias trigger is the level-one trigger that records the most of our Au-Au data. The collision vertex and the number of hits in the BBC photomultipliers are key variables for the PHENIX minimum bias trigger.

## 2.3 Central Arms Detectors and Single Particle Measurement

The following will be an introduction of Pad Chamber (PC), Drift Chamber (DC), Ring Imaging Cherenkov Detectors, Central Arm Magnets, as well as how they work as single particle detectors. The particles that we are interested in include high energy $\pi^0$ as trigger particles, since it is highest-$p_T$ identified particle, charged hardrons as associated or conditional particle. The combinations of detectors are used to reconstruct the particles of interests and to remove the background, i.e. the "fake" particles.

### 2.3.1 Central Arm Magnet

The central magnet is composed of two pairs of concentric coils and provides an axially symmetric magnetic field parallel to the beam and around the beam axis. Charged particles bend in a plane perpendicular to the beam axis. The bending angles are accurately measured by the DCs on the edge of magnetic field, then, the momenta of the charged particles can be calculated.

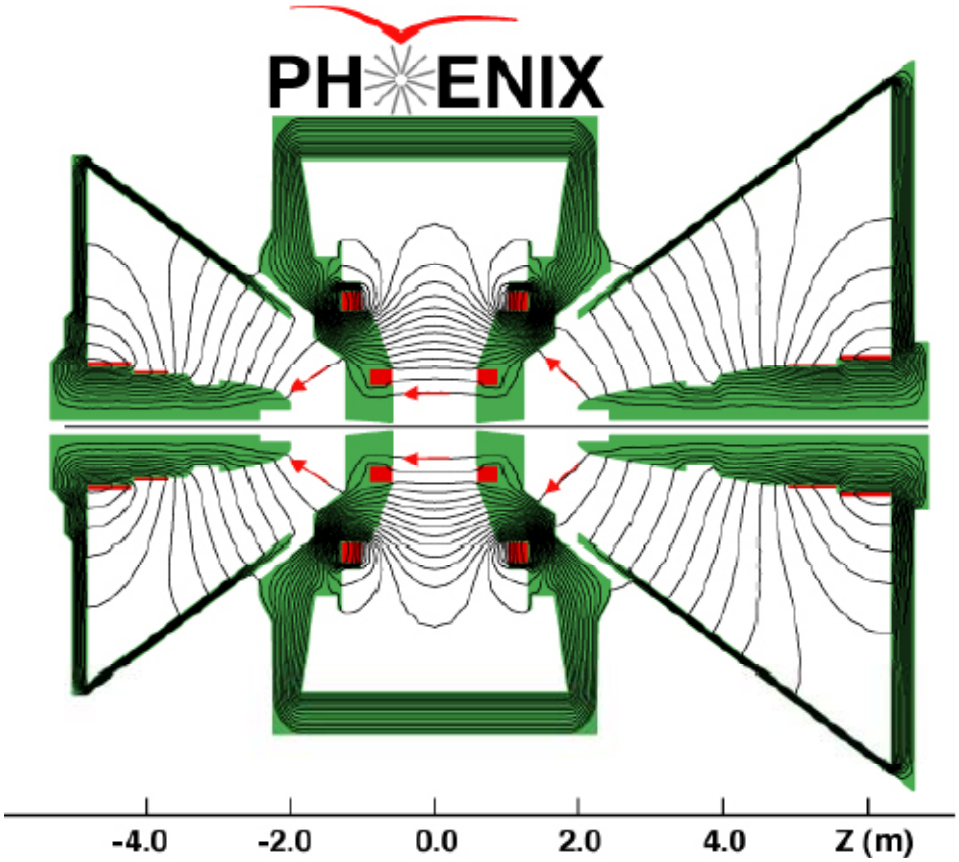

Fig2.3 Magnetic Field Lines Distribution with outer Central Magnet Coil Engergized.

### 2.3.2 Drift Chamber

The two PHENIX drift chamber are cylindrical, each cover $\pi/2$ in azimuth and 1.80m long in z direction centered around midrapidity. DCs are located on the edge of the magnetic field, from 2.02m to 2.46m (radial distance from beam axis). When charged particles travel through a drift chamber, they ionize the gas mixture (50% argon, 50% ethane with <1% alcohol). The hit position is measured by the time the released electrons hit the sense wire. The function of drift chambers also includes measurement of the azimuthal angle of the tracks.

Each drift chamber (east or west) consists of 20 sectors, each with six wire layers: X1, U1, V1, X2, U2 and V2. Fig. 2.4 shows a side view of a single sector. There are four types of wires in the drift chamber as shown. Potential wires create the drift electric field in the detector. The sense wires collect the signal charge for the hits. The gate wires further shape the field to direct the charge toward the sense wires from one side. The back wires block charge from the other side from reaching the sense wires. This prevents ambiguities in the hit position. The U and V wire layers are oriented at an angle 6 degree, with respect to the X layers; opposite ends of the U and V layers are in neighboring sectors.

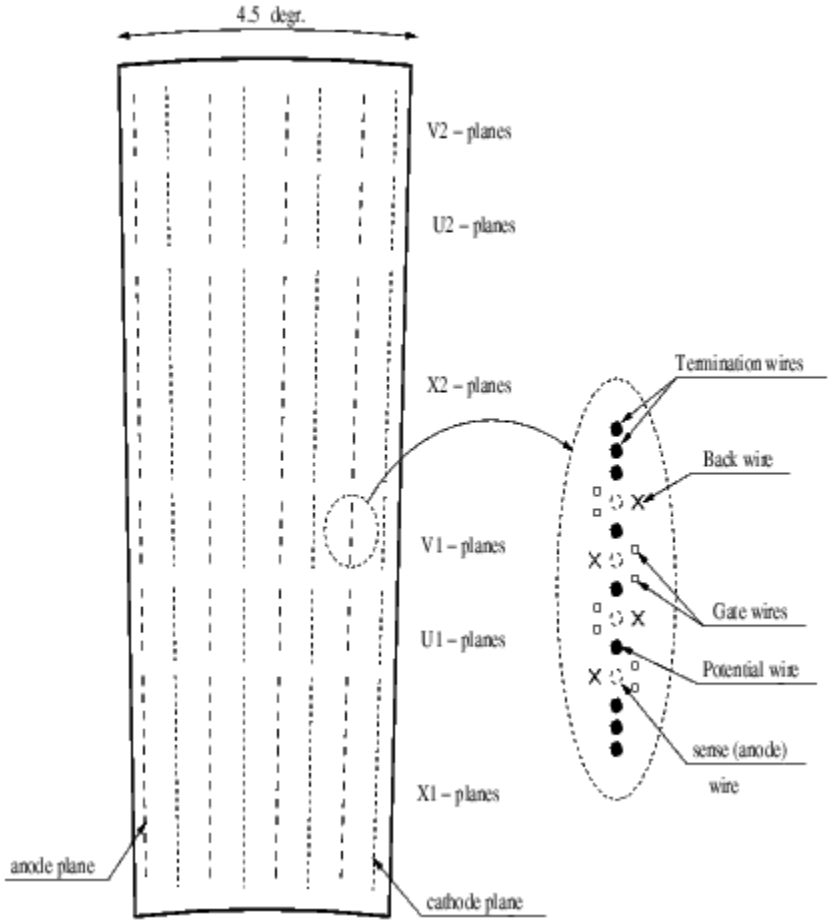


Fig 2.4 Side view of a drift chamber sector showing the positions of the wire layers. Also shown is the wire positions for the V1 layer (other layers are similar).

The U and V layers are designed for hit position measurement on z direction. DCs has resolution better than 0.15mm in $\phi$ direction, better than 2mm in z direction, and track separation better than 1.5mm.The single wire efficiency is 95%; the single track efficiency is larger than 99% .

Momentum measurements are made by measuring the tracks angular deflection from a straight line, $\alpha$ (see Figure 2.5). $\alpha$ is inversely proportional to the track momentum since axial magnetic field is approximately uniform. During reconstruction in DC, Tracks are transformed into 2-dimension $\phi - \alpha$ space. All hit combinations are plotted in $\phi - \alpha$ space where good quality tracks show up as peaks. More information about the drift chambers can refer to [19].

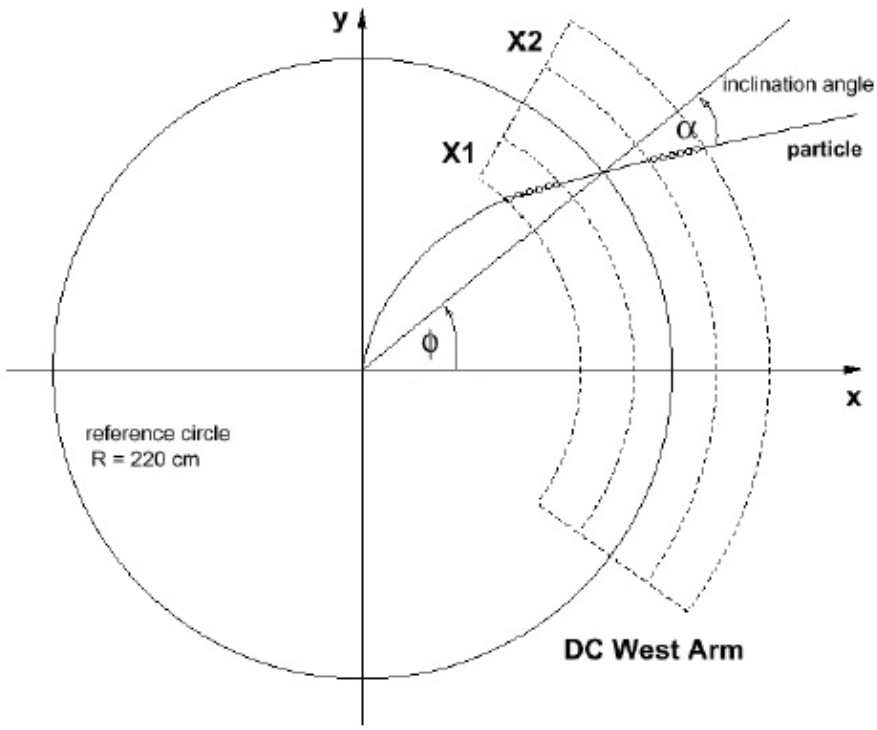


Fig 2.5 A drawing of tracking parameters for the drift chamber. α is the track's deflection from a straight line and ϕ is the azimuthal angle of the track measured at the drift chamber reference radius of 220cm.

### 2.3.3 Pad Chambers

After reconstructed by DC, charged tracks are then projected onto three layers of multi-wire proportional pad Chambers (PCs). Each PC is a single plane of wires bounded by two cathode planes, one of which is segmented into pixels. The pad chambers consist of three layers in West Arm (PC1, PC2 and PC3) and two layers in the East Arm (PC1 and PC3). The matching of DC tracks with PC hits can be used to remove backgrounds including conversions, and decays. Because all charge tracks are reconstructed with assumption that

they are from collision vertex, “noise” tracks is unlikely from collision vertex and their momentum vector are unrealistic. The hit efficiency is greater than 99.5% in PCs, the z resolution is 1.7mm.The two-track resolution for PC1 and PC3 is 4 cm and 8 cm, respectively. More information about the Pad Chamber system can be found in [19]. Fig2.6 is the 3D view of PCs.

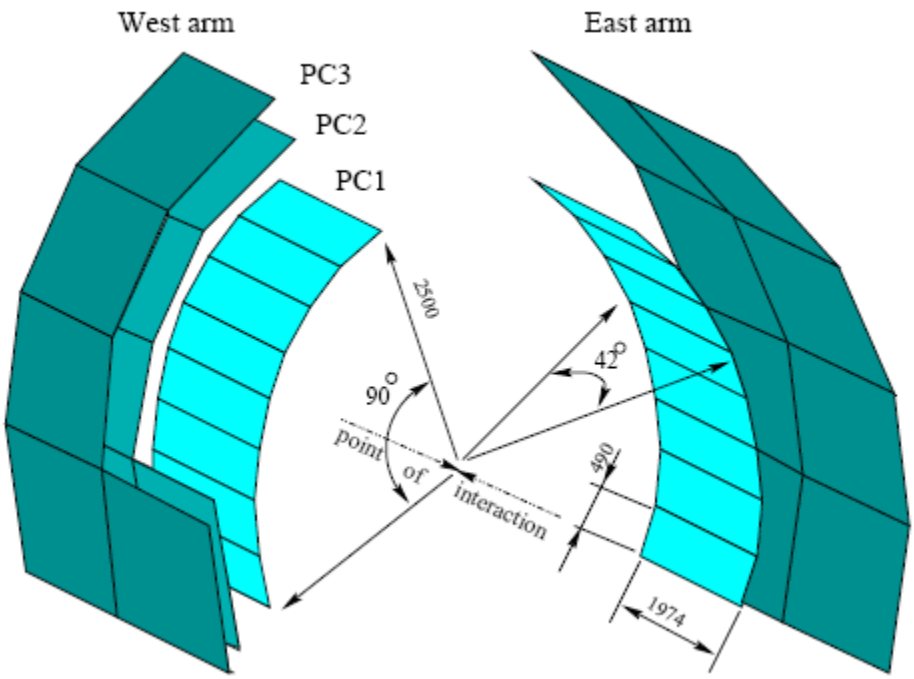


Fig 2.6 3D view of PCs.

### 2.3.4 Electro-Magnetic Calorimeter

EMCal is mainly designed for electron identification, direct photon measurements, neutral meson (e.g. $\pi^0, \eta$) measurements via their $\gamma\gamma$ decay channel, and low $p_T$ charged hadron identification from their time-of flight. However, since the two types of calorimeters have 0.85 units of hadronic interaction length, high $p_T$ charged hadrons also have a large

probability of depositing a large fraction of their energy. Thus they can provide a background veto for charged hadrons.

EMCal covers the all the central arm acceptance with 2 types of calorimeters, Lead Scintillator (PbSc) sampling calorimeters and Lead Glass (PbGl) Cherenkov calorimeters. There are 4 sectors of PbSc in west arm, 2 sectors of PbSc and PbGl in the east arm. Both detectors have very good energy, spatial and timing resolution, while the PbSc excels in timing and PbGl in the energy measurement [20].

### 2.3.4 Ring Imaging Cherenkov Detector

If a charged particle's speed in medium is larger than the light speed in the same medium, it will radiate Cherenkov light to be detected by RICH. The threshold transverse momentum for electron is above 10MeV/c, for charged pions ($\pi^0$) is above 4.9 GeV/c. This Cherenkov light is reflected off the back of the RICH by a set of mirrors that focus the light onto a series of PMTs to be read out [21].

# CHAPTER 3. DATA ANALYSIS

In the following Section, I will introduce the global event selections and single particle selection. My work is mainly about how to choose the most reasonable data for particle reconstruction. The single particles include the $\pi^0$ trigger particle and charged hadrons. Charged hadrons are grouped into associate hadrons and conditional hadrons respectively.

A "run" refers to a short period, about 1 hour of PHENIX data taking for which the detectors and beam conditions are very stable. The start of the next run is manually decided by the operator on shift, if the operator judge that the current experiment is in a good status to start. A "Run" refers to a year of RHIC operations.

In order to keep physics events of interest within a valid experiment condition for quality assurance (QA), several real-time experiment parameters are used to label each run. These parameters include magnetic field configuration, beam luminosity, level-one trigger rates, and when applicable the spin configuration. Then these parameters are applied during the physical run by data acquisitioning system (DAQ) operation, to obtain a consistently uniform performance of detectors. This is also called "on-line" calibration, contrary to the "off-line" calibration later done to the reconstructed data. The 1-hour period makes calibration work based on a short time interval and give more stable and consistent output. For later analysis, the data is from varied collision systems, each collision systems have its own selection.

## 3.1 Run & Event Selection

First, we applied general cuts to all events. We only reconstructed event from collision vertex (by BBC or ZDC) within -30cm to 30 cm. After the run-QA step, Au-Au collision events are divided into centrality bins. Because more central the collisions are, higher per-event trigger yield is contained. The choice of the event division is to make sure statistics is enough in each bin, along with the drive to have narrow bins that are more similar in geometry. Since the peripheral events has lower per-event yield, the more peripheral bin is usually wider.

Run QA is based on the criteria to minimize the effect of detector performance fluctuation, by setting cuts on averaged event information over the whole run. This averaging method avoids, to some extent, loss of rare events that truly contain the physics we are interested in (e.g. hard-scattering). These averaged event information are recorded and plotted on a run-by-run basis, and we calculate the threshold based on such a plot. If one run has its variables out of threshold, the whole run is abandoned. One optimal way to calculate the threshold is to directly compare between runs. For instance, if events are under same collision systems, the mean $p_T$ per event, if taken averaged over the whole run, should fall in a small range for all runs. Then we can abandon runs with a too high or too low mean $p_T$ typically as showed in Fig.3.1.

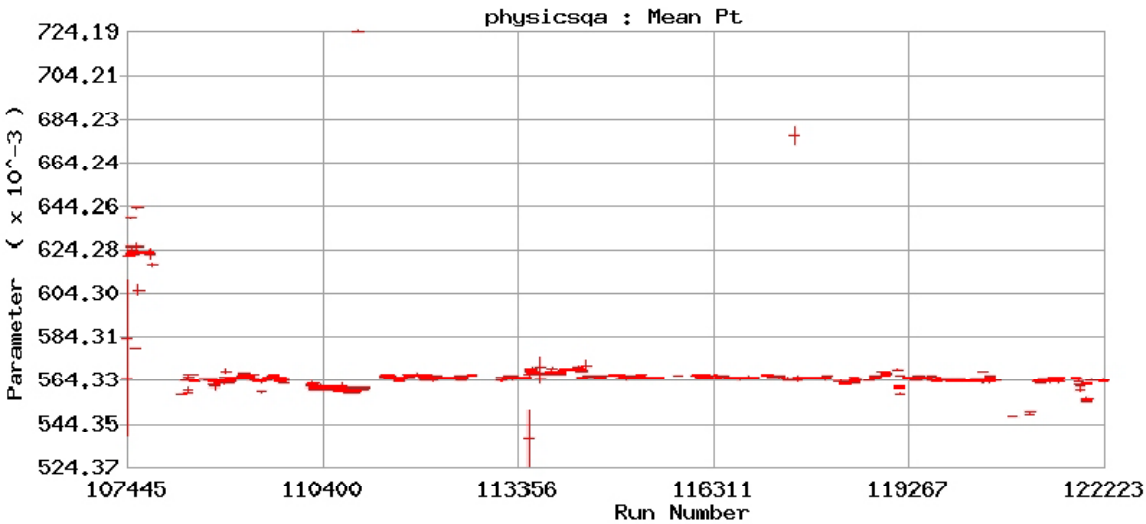


Fig. 3.1 A run-group threshold plot, run numbers verse run-mean-$p_T$ distribution, generated by the calibrators database.

Another way is to plot distributions inside one run. For example, the distribution of centrality is supposed to be purely random and to be flat. It's quite natural to decide to throw away a run if its centrality distribution clearly deviates from a flat line. Fig.4.2 is a typical "bad" run based on this criterion. This quality check shall be done in the min-bias data of PHENIX.

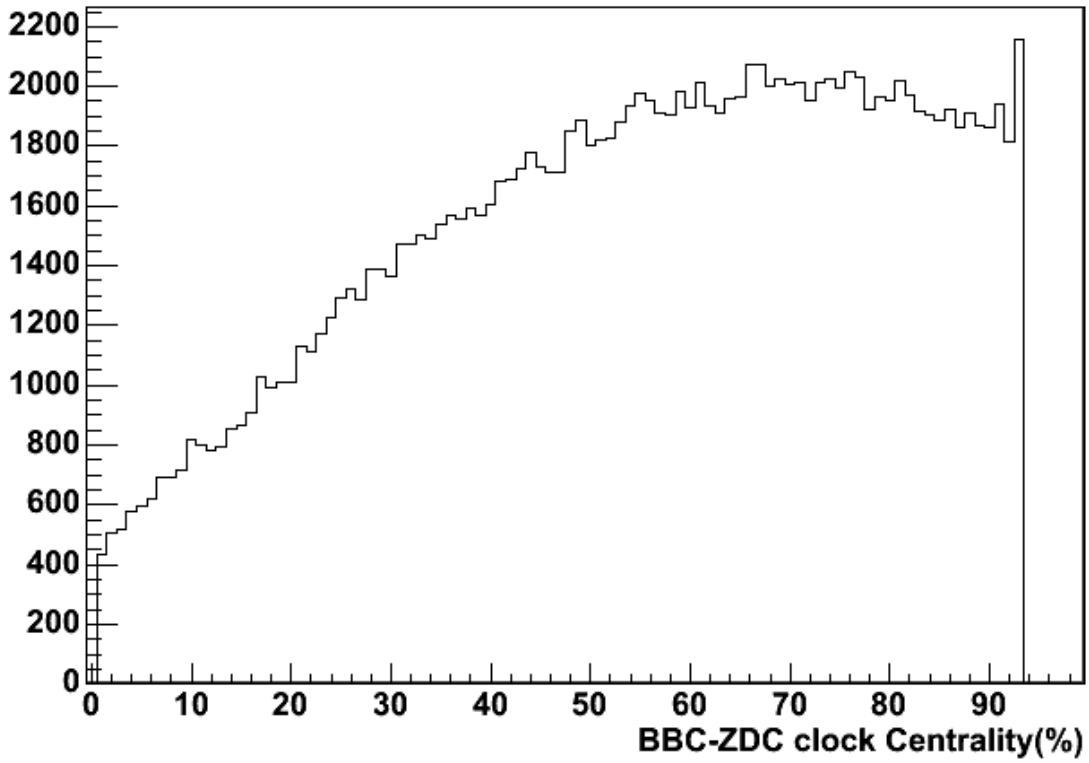


Fig.3.2 A typical "bad" run is shown here. Centrality distribution is obviously deviated from a flat line

## 3.2 Single Particle Selection

As mentioned in Chapter 2, for "2+1" correlation, a high-$p_T$ charged hadron as conditional particle is needed in the same event that already contains a valid high-$p_T$ $\pi^0$ trigger particle. The absolute value of relative azimuthal angle between this hadron and the trigger $\pi^0$ is larger than $\pi/2$, which means in the back hemisphere of trigger particle. The following subsections are focusing on the single particle selection algorithm. I will show the different effect of detectors and decide how to combine best cuts for particle reconstruction.

Hadrons that decay before the DC or electrons/positrons from photon conversions close to DC can mimic high momentum tracks. This is because the daughter particles usually change the flight direction due to decay kinematics and they do not bend much since the

magnetic field is very weak after the decay point. Those particles can end up reconstructed in DC as high momentum particle, whereas their real momentums are small. It is difficult to distinguish on a track-by-track basis whether a given track is primary or from decay. The tracks that we are interested in come from the primary collision between two Au nulei. One main part of this thesis work is to figure out how to remove as many of the background tracks without removing too many of the primary particles.

### 3.2.1 charged Particle Selection

A primary method to remove electrons is to project the charged tracks to RICH radiation rings. Any charged pion/kaon/proton with a $p_T$ < 4.9GeV/c won't radiate Cherenko light in the PHENIX RICH detector, and has thus $n_0$ coincidence with RICH radiation rings ($n_0$<=0). This works as a good cut for our charged tracks below this $p_T$ threshold. Further cuts in DC and PC3 are made on the tracks used in this analysis to ensure as little contamination from background as possible.

#### 3.2.1.1 Track Quality Cut

Charged particles are reconstructed as DC/PC tracks. The quality of a track is assigned a 6-bit word to represent the information used in the reconstruction. From low to high, each bit means:

bit 0: This track has hits from X1 wire layers,

bit 1: This track has hits from X2 wire layers,

bit 2: The presence of hits in the UV layers,

bit 3: The uniqueness of hits in the UV layers

bit 4: This track has matched PC1 hits (falling within the window of the DC track's projection to PC1),

bit 5: This track has a uniquely matched PC1 hits.

Tracks used in this analysis are required to have hits in X1,X2, UV and PC1, which means quality is larger or equal to 31. There won't be arbitrary combinations of all bits in track quality as shown in Fig.3.3 .For example, a DC track has to have both X1 and X2 hits to be reconstructed. The stored ntuple is for quality > 7.

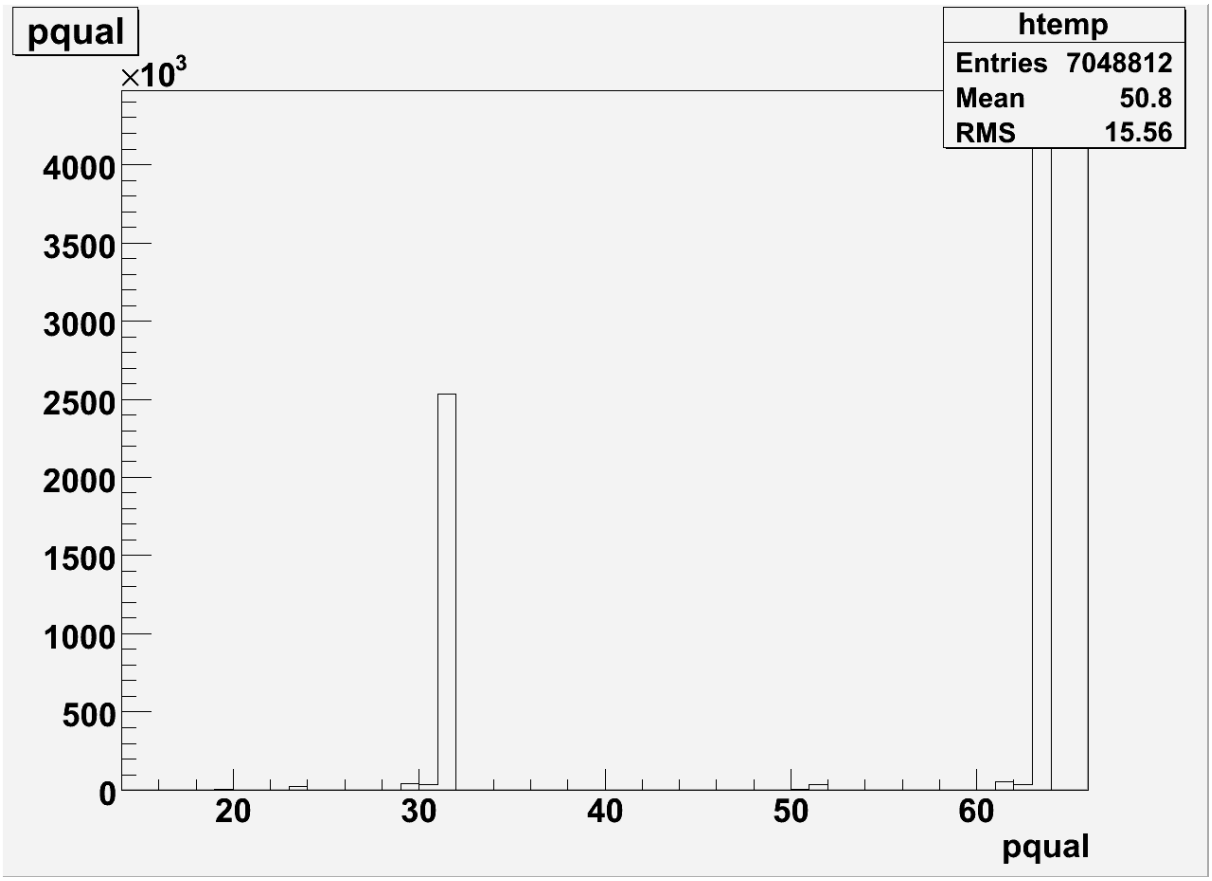


Fig .3.3 The plot of Quality. Qual==31 and qual==63 are dominated.

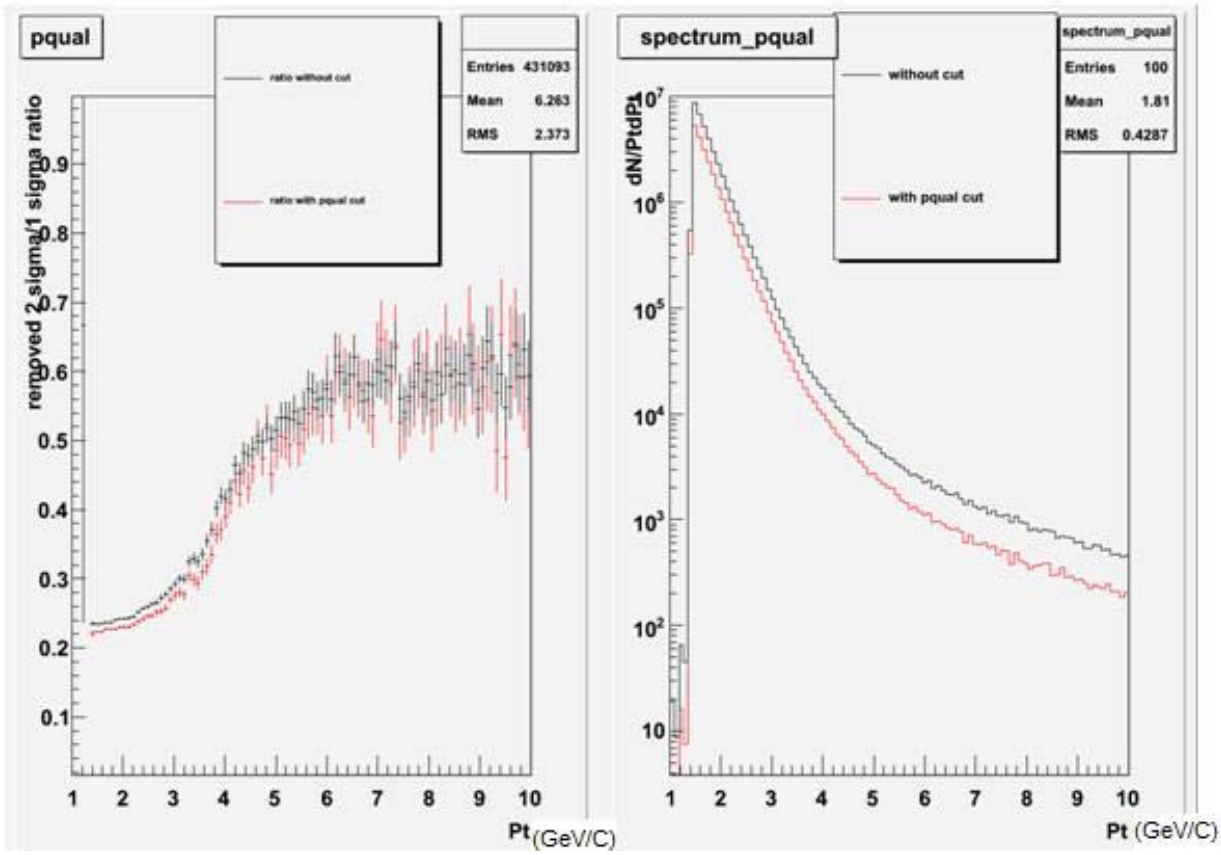


Fig 3.4. Single quality cut effect plot. The left panel is the plot of ratio of number of events removed by 2 sigma square cut on PC3 over 1 sigma square cut. The right panel is the spectrum of charged hadrons. The red line is after applying the quality cut (pqual==63), the black line is without any cut for comparison.

Many of the conversion products that reconstruct as high-$p_T$ particles are really low-momentum particles. They are reconstructed as high-$p_T$ tracks since they convert outside the region where the magnetic field is strong. Since these are low-$p_T$ particles they will multiscatter more between the drift chamber and PC3. Hence if we project each track from the drift chamber to PC3 the background particles are likely to have a PC3 matching hit that is further away from the central projection. The matching variables are normalized to be a normal Gaussian, centered at 0 and $\sigma = 1$, see Fig. 3.7.

We calculate how many tracks are removed by a 2-sigma cut on PC3 compared to how many tracks are removed by a 1- sigma cut. If this ratio is flat with momentum, then the sample of tracks is likely to be normal and dominated by tracks that really have that reconstructed high-$p_T$. If this ratio begins to increase, then more background tracks that really have low-$p_T$ are entering into the sample. Hence the goal is to find cuts will produce a removal ratio, 2-sigma/1-sigma, that is flat out to as high as possible.

Fig. 3.3 shows the spectrum of quality, while Fig. 3. 4 shows the comparison of data before and after quality cut. In Fig. 3.4, the rising of the line in left panel implies that the background starts to dominate in the data set. We can see that the quality cut reduces the background, but not significantly. The theoretical value of the ratio is about 17%, the higher value shown in Fig. 3. 4 is due to the correlation data as 2-dimension Gaussian. The line starts to rise at around 2.5 GeV/c in $p_T$

#### 3.2.1.2 Drift Chamber Zed Cut

Because the hits on the edge of DC detector might cause unreliable reconstruction and that there is more material near the edges to produce conversion, we applied a cut on the Z-coordinate of hit position –zed in DC, where zed is the distance from the center of the interaction region along the beam pipe direction at DC. The drift chamber extents to |pzed|=80cm.the stored ntuple is |pzed|<75 cm.

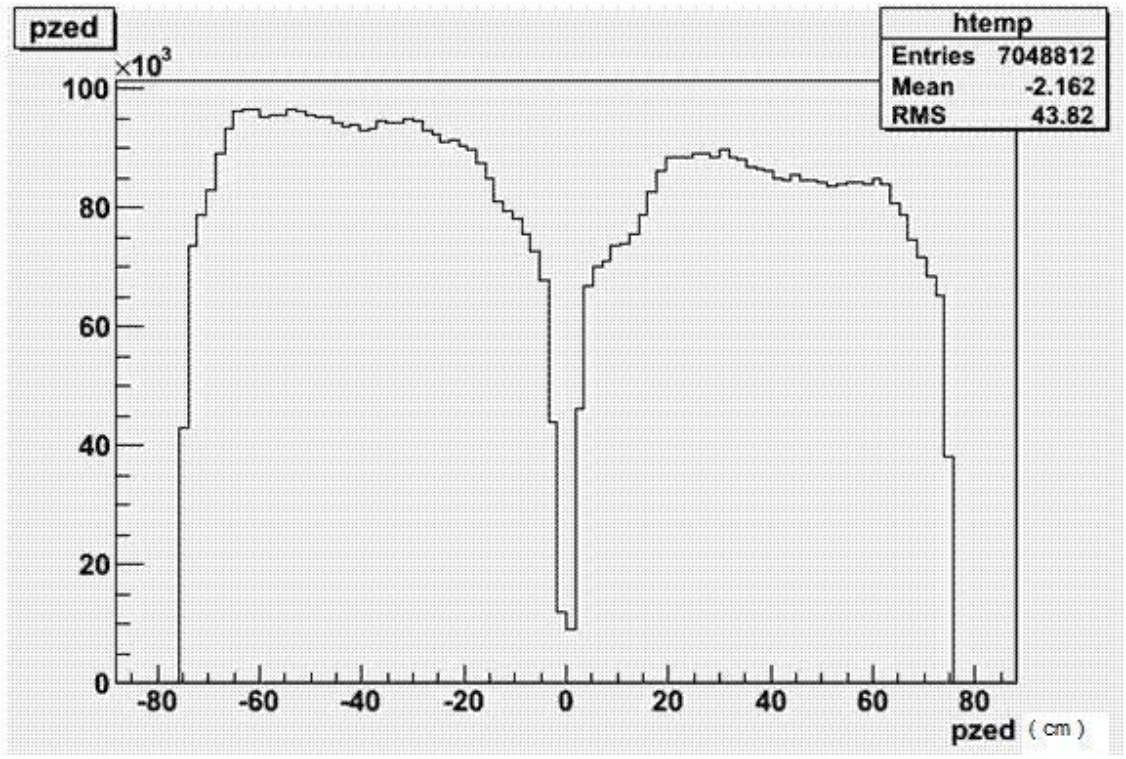


Fig.3.5. Z position in DC with cut |pzed|<75 cm. It's almost flat in both positive and negative region which corresponds to the randomness of hitting in DC.

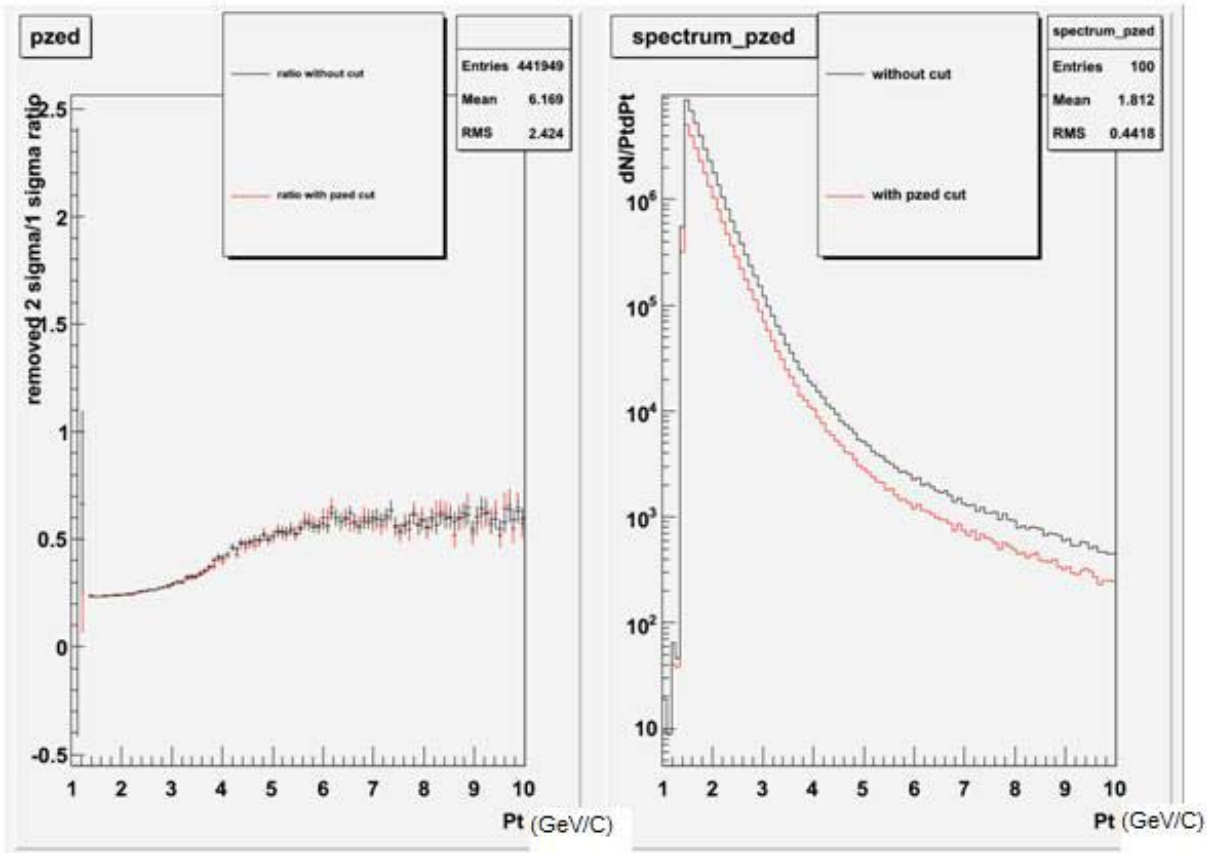


Fig.3.6. Single zed cut effect plot. The left panel is the plot of ratio of number of events removed by 2 sigma square cut on PC3 over 1 sigma square cut. The right panel is the spectrum of charged hadrons. The red line is after applying the zed cut (|zed±20|<40 cm), the black line is without any cut for comparison.

Similarly, Fig.3.5 and Fig. 3.6 show the spectrum of zed, and the comparison of data before and after cut. We can see that the zed cut barely remove the background. It's because the default cut had removed background near the edges when we stored the data.

### 3.2.1.3 Matching at PC3

Unidentified charged hadron tracks are matched to hits in PC3. The distributions of the distance of the track projection, its position at DC and hit position in PC3 is fit to a Gaussian. We don't use PC2 because it's only installed at west arms. The distances are measured in two dimensions, z and $\phi$. The shapes of Gaussians vary with respect to $p_T$ range. Low $p_T$ tracks have broader distributions than high momentum tracks.

Random combinations between DC/PC1 hits and PC3 hits will make noise to their distributions. The Gaussian of random combinations can be derived by swapping North/South sectors of DC/PC1 to PC3 correspondence. That is, we swap the sign of z-coordinate of south PC3 hits and match them to the projection of north DC/PC1 and vice versa. Because there can't be any real physics between such combinatorials, the shape of such "swapped" matching deviation shall be the pure background combinations. Then both pairs of Gaussians are normalized and written into data. These variables are called ppc3sdp/ppc3sdz. Naturally, such distribution shall always be a normal Gaussian, centered at 0 and $\sigma$ =1, see Fig.3.7.

In our following analysis, we require a $2\sigma$ PC3 matching, which is $\sqrt{\Delta\phi^2 + +\Delta z^2} < 2$, $\Delta\phi$ and $\Delta z$ coordinates are in unit of $\sigma$ of Gaussian. This will include most "real" charged tracks, while efficiently remove those obviously unreasonable matchings.

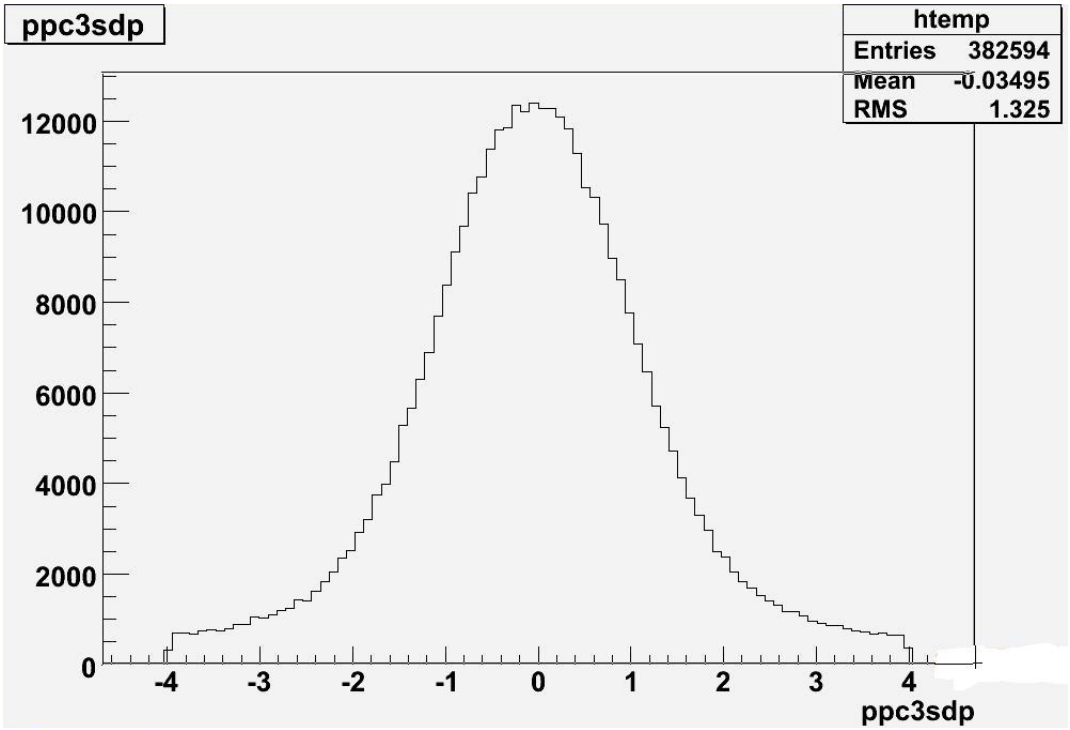

Fig.3.7 An example plot of PC3 matching distribution of DC/PC1 tracks in $\phi$ direction.

### 3.2.1.4 m2emc Cut

There are time of flight detectors in the EMCal, which can measure traveling time of the particles, and we know distance between the collision vertex and hit position, velocity can be known, and with the reconstructed momentum, we can calculate the mass square of a particle. Fig.3.8 shows the $m^2$ of identified particles in the EMCal. The first peak around zero are the charged pions, the peak around 1 is proton. We applied the cut -0.5 GeV<$m^2$<1.5 GeV to include all these particle of interest. The long tail contains the information of the background, when we applied the cut, we cut the background too. Fig.3.9 shows the effect of the cut on reducing the background. The raising indicates the increasing dominance of background.

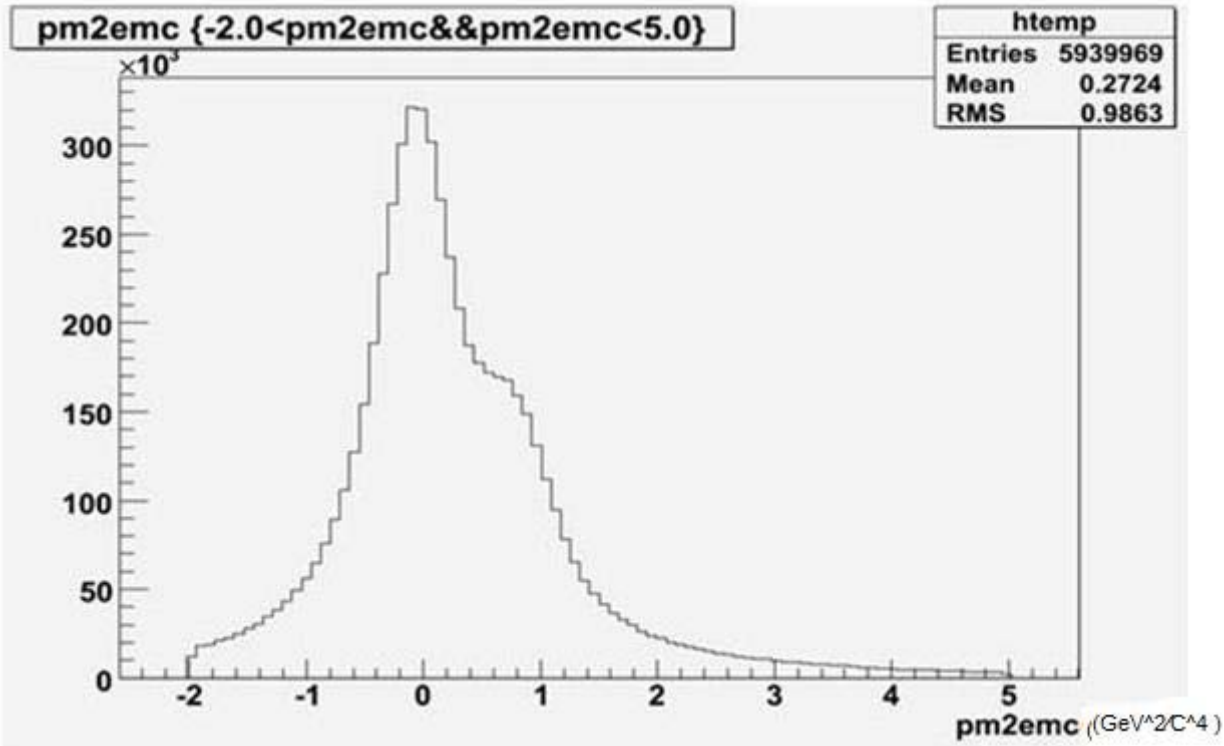


Fig.3.8 a typical plot of $m^2$ distribution in EMCal. The first peak is for pion. The second peak is for proton. The x axis is the $m^2$ in EMCal.

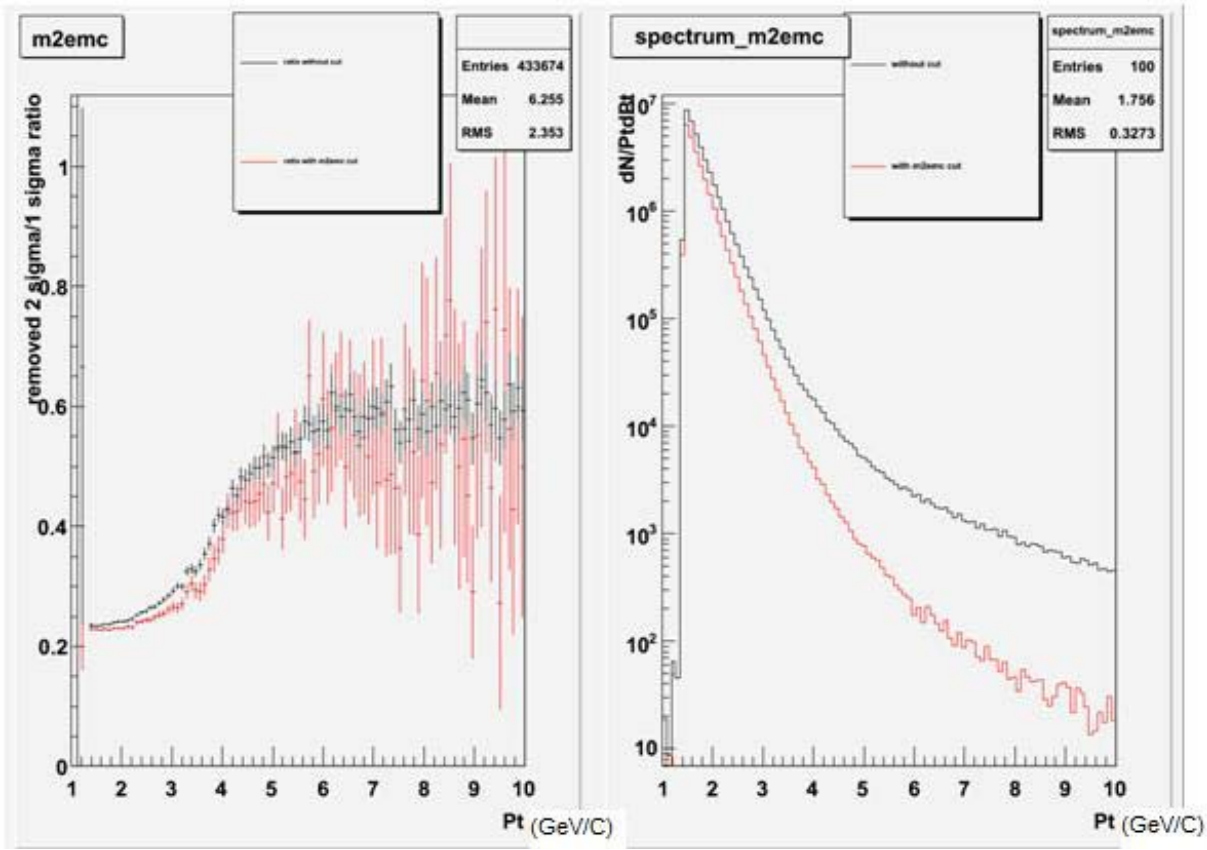


Fig. 3.9. Single m2emc cut effect plot. The left panel is the plot of ratio of number of events removed by 2 sigma square cut on PC3 over 1 sigma square cut. The right panel is the spectrum of charged hadrons. The red line is after applying the m2emc cut (-0.5<m2emc<1.5Gev), the black line is without any cut for comparison.

Fig.3.8 and Fig. 3.9 show the spectrum of m2emc, and the comparison of data before and after m2emc cut. We can see that the m2emc cut improve the background, but not significantly as well. The line starts to rise at around 3.0 GeV/c in $p_T$ .

### 3.2.1.5 EP cut in EMcal

EMCal can also be a good detector of the hadronic deposited energy measurement in EMCal. A fairly strong method of removing background at low $p_T$ region is called ep cut in my thesis, which is keeping data satisfies E>0.3+0.15*P.

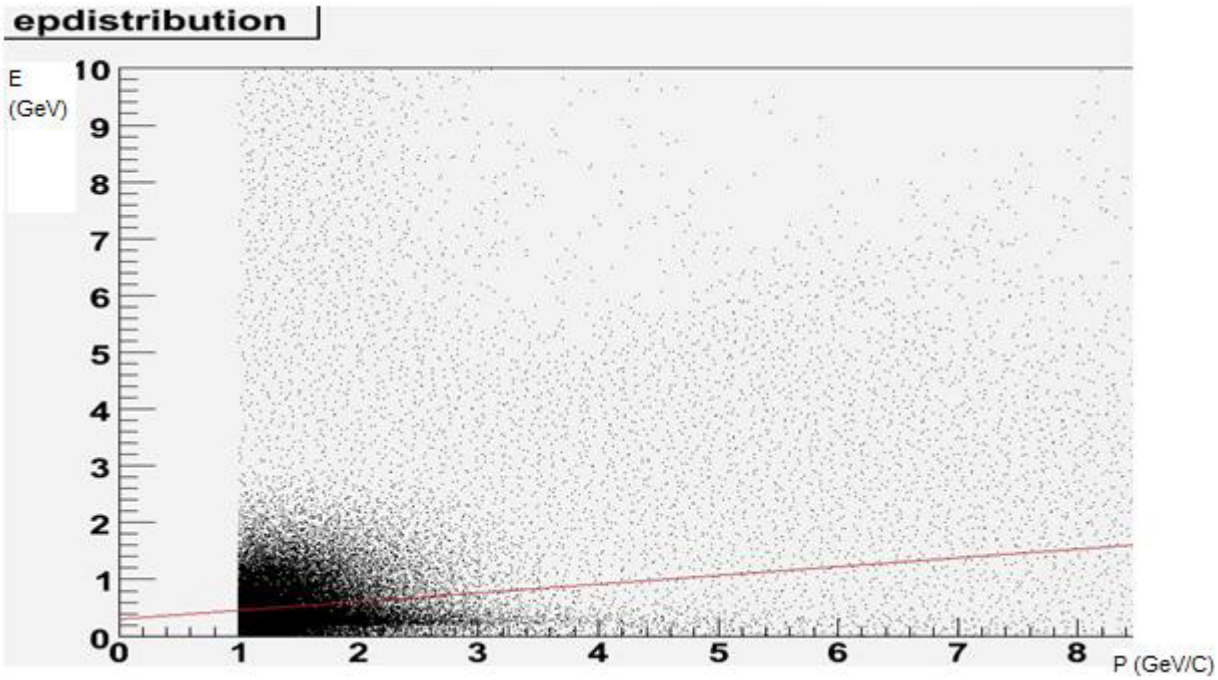


Fig.3.10 Energy-momentum distribution. Red line is e-0.3-0.15*p=0. E is y axis and p is momentum as x axis.

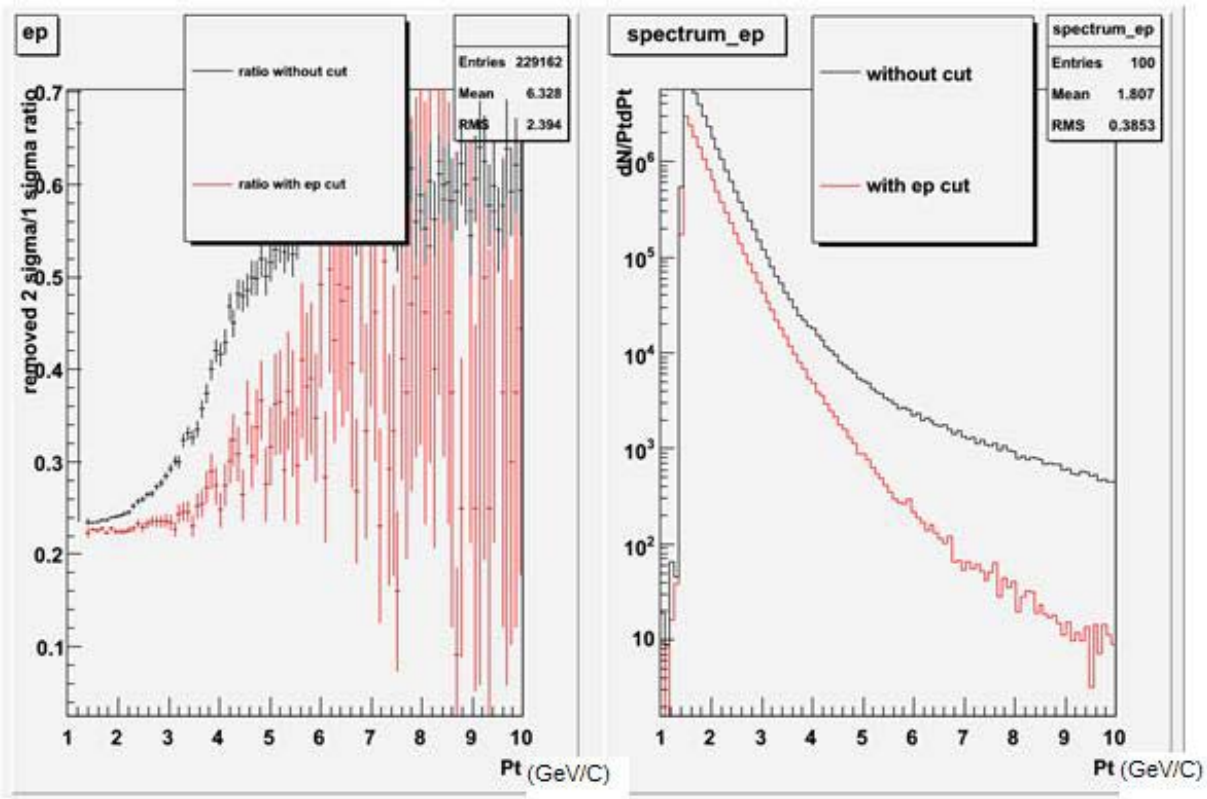


Fig.3.11 Single ep cut effect plot. The left panel is the plot of ratio of number of events removed by 2 sigma circular cut on PC3 over 1 sigma circular cut. The right panel is the spectrum of charged hadrons. The red line is after applying the ep cut(e-0.3-0.15*p), the black line is without any cut for comparison.

As shown clearly in Fig 3.11, the ep cut is very strong in removing the background. The background starts to dominate at around 4 Gev, much better than other cuts.

Table 3.1 shows the effects comparison for different cuts. I will pick 2 promising cut from them. Promising cut means when we apply this cut, it effectively removes a large fraction of the background. Ep cut has the highest $p_T$ value where the removal ratio 2-sigma/1- sigma begins to rise, hence we pick ep cut as the most effective cut. The second effective cut will be m2emc cut, cause it has the second highest $p_T$ value where the removal ratio begins to rise.

Tab. 3.1 Effectiveness comparison between different cuts.

| Cut name | Fitting ratio at flat region | Rising Pt(condition on fluctuating between 0.9 ratio,1.1ratio) | # of all tracks after cut/# before cut (condition on Pt< Rising Pt) | Analysis |
|---|---|---|---|---|
| Ep cut:E-0.3-0.15*ppt>0 | 0.227 | 3.6 | 35.51% | Most promising cut, cut lots of background, and has the largest Rising Pt, and m2emc cut has the second largest rising Pt. |
| M2emc: -0.5<m2<1.5 | 0.227 | 2.7 | 65.85% | |
| Qual: pqual==63 | 0.224 | 2.5 | 60.66% | |
| Zed: Fabs(zed+-40)<20 | 0.234 | 2.3 | 58.20% | |

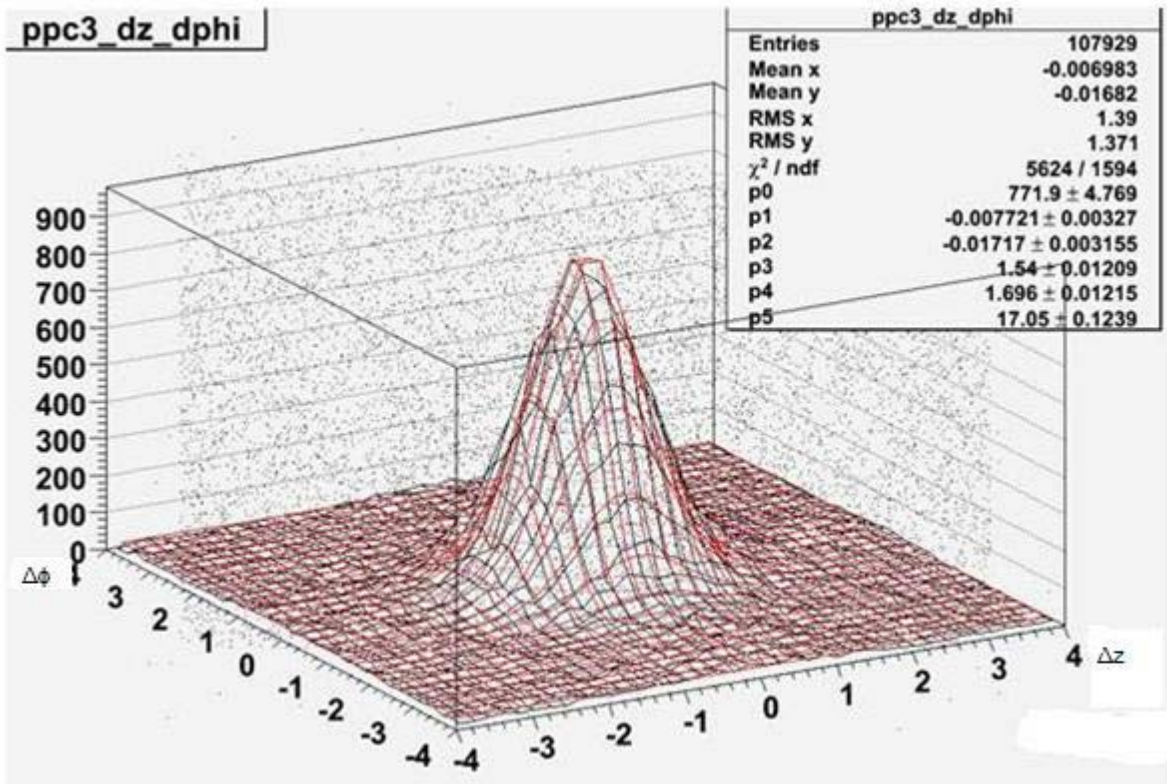


Fig.3.12 2-dimension plot of PC3 in $\phi$ and z. The red shape represents for the fitting function. With m2emc cut, ep cut, ratio of S/(S+B) with $\Delta z^2 + \Delta\phi^2$<4 is 99.14%.Red shape is the fitting function, black is data we measure. The black dots are random junk we can not get rid of.

With these cuts we then projected the selected sample of tracks onto the two PC3 matching variables. The goal to try to estimate how much background is remaining after the cuts. In Fig.3.12, I fitted the data with a 2-dimension Gaussian function plus a flat constant as background. The background is not known, but we can assume reasonably it's a Gaussian function with large width, and we can think in the fitting region, it can be treated as a constant. From this fit we calculate the S/(S+B) ratio where S is the signal of the fitted Gaussian within a 2-sigma radius and S+B is the whole data within the radius. S/(S+B)=99.14% means that less than 1% of the tracks within a 2-sigma window seems to be

background tracks, i.e. the cuts are good to remove much of the background. The plot is under $p_T$ range of 3 to 4 GeV, this is also the region for conditional particle. The fitting function is $[0] \times \exp\left\{-\frac{(x-[1])^2}{2\times[3]} - \frac{(y-[2])^2}{2\times[4]}\right\} + [5]$, [n] is the fitting parameters.

### 3.2.2 $\pi^0$ Selection & Photon Selection

Because $\pi^0$ has 99% probability of decaying to γ pairs, we use them to reconstruct $\pi^0$ .

#### *3.2.2.1 Photon Selection*

Electrons/photons, which form a spray of electrons and photons in EMCal, will radiate light and be collected by EMCal towers. The spray is produced by photons which entered EMCal detector. Usually one particle will create a shower that is collected by more than one tower. One cluster's energy distribution among towers drop dramatically from center to edge, thereby we use 21 towers, 5x5 without 4 corners, to reconstruct one particle. We will loop through the towers, find energy peaks (center tower of shower), and form clusters using towers around each energy peak. Photons usually need all 21 towers to collect almost all the energy, while hadrons may need only the central 3x3 towers. We need to evaluate the quality of each cluster. The existing parameters include:

1) Energy distribution shape: We use $\chi^2$, the difference between measured and expected cluster shape. $\chi^2$ is defined as $\chi^2 = (\sum_i(\frac{E_i^{meas}-E_i^{pred}}{\sigma_i})^2)/ND$, i is the tower, and $E_i^{meas}$is the measured energy, $E_i^{pred}$, $\sigma_i$ both depends on measured energy, ND is number of degree. We use $\chi^2 < 3$ cut for photons in Fig.3.13. Another advantage of this χ2 cut is to remove overlapping PbSc clusters, which will give a large $\chi^2$. In our dynamic region where most pi0 $p_T < 10GeV/C$, it's rare for two photons from same

$\pi^0$ to overlap at EMCal. So overlapping clusters can be viewed as pure noise, such as random combination of two un-correlated photons.

2) Time-of-Flight (TOF). The massless photons/electrons shall reach the EMCal (Distance ~5m from collision vertex) within D/c = 20ns. The heavier hadrons within the same $p_T$ region will arrive later. It then takes all particles a finite time to produce EMCal shower and radiate light. This means the $\mathrm{TOF} = t_{\mathrm{EMCal}} - t_{\mathrm{BBC}}$ will have a distribution as a sharp peak below 100ns and a long broadened tail. In our analysis, we are using only the lower limit of TOF to cut off unreasonable EMCal response (TOF> −400ns) and rely on the shape cut to remove those hadrons from our $\pi_0$ samples. These unreasonable EMCal responses are usually from either tail of last bunch cross, or the hot channels of electronics.
3) Dead/Warn map cut. The EMCal tower electronics sometimes doesn't work fully well. One tower may become too hot (count at too high a rate) or dead. If a tower is too hot, it will make lots of noise, which will be treated as lots of clusters and mistakenly reconstructed, and if a tower is dead, it might miss lots of real clusters' information. Thus photon coming of such tower is not reliable. We make a dead/warn map of EMCal towers, and require that any photon we used cannot be from this map.

The cuts for single photon are listed here:

$\chi^2 < 3$,

EMCal time-of-flight > −400ns,

photons can't be from EMCal areas marked as warn/dead.

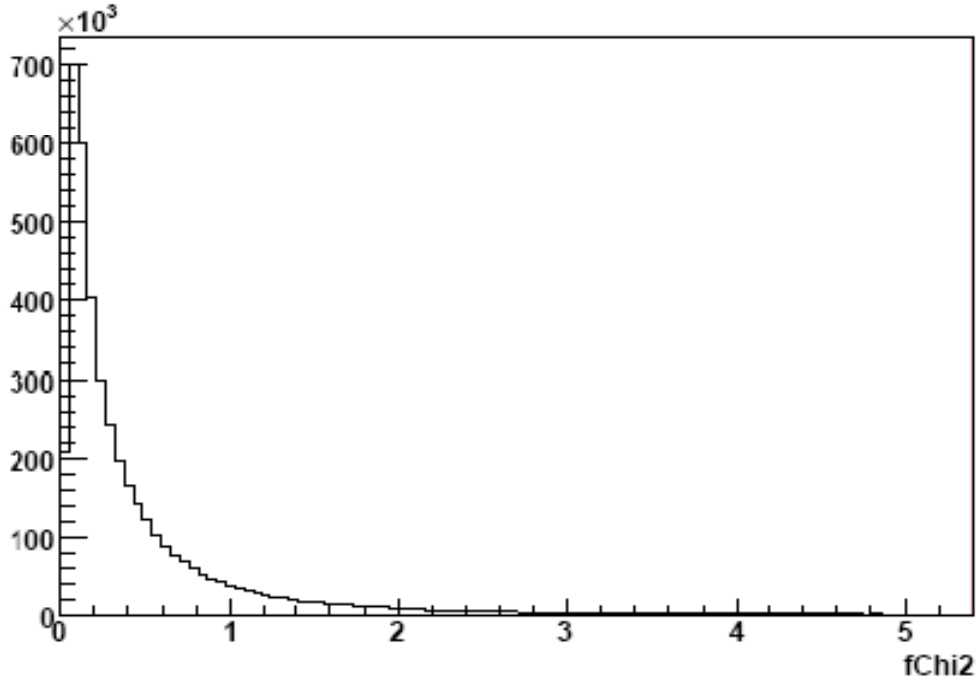


Figure 3.13 An example plot of EMCal $\chi^{zf}$ distribution.

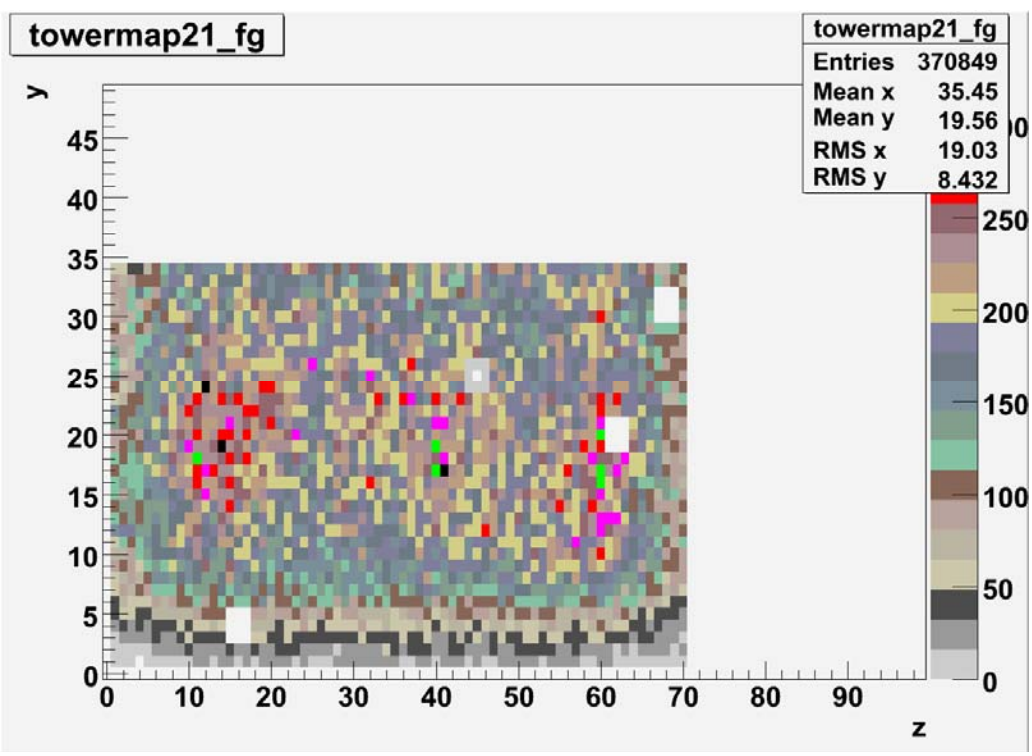


Fig 3.14 a typical tower map for one sector in EMC, Each tiny squares in the plot represent one EMCal tower.

### *3.2.2.2 $\pi^0$ Selection*

In order to have a reasonable high $p_T$ $\pi^0$ trigger tag the jet, we need to achieve as much high signal-noise ratio(S/B) as possible when selecting $\pi^0$. The invariant mass of pi0 are reconstructed from the two photons. A typical distribution of invariant mass of pion is as in Fig. 3.15. One part of my thesis is to find ways to reduce the random combinations making the background within the mass region of the $\pi^0$

Note the energy measurement of photons can deviate from real values. And there can be random combinations of photons whose invariant masses fall nearby the published $\pi^0$ mass. Therefore, we need to apply a cut to determine the reasonable invariant mass range. The standard method in PHENIX is to fit this spectrum using addition of two shapes: Gaussian as the "real" $\pi^0$ plus a 3rd order polynomial as combinatorial background. The center and σ of Gaussian varies with $p_T$ and centrality. In practice, we made a fixed cut of $|\pi^0$inv_mass -1.4|< 0.02GeV/$C^2$. In the high $p_T$ (>5GeV/c) region we studied, the peak positions and Gaussian widths are mostly stable and this is a safe cut.

At high-$p_T$ region, combination of one high-$p_T$ photon from a real high-$p_T$ pion and a low energy photon from unknown source is the most ordinary way of reconstruction of "fake" pion. To remove the random combinations, another method is to apply the asymmetry cut. The asymmetry is defined as $\text{asymmetry} = \frac{|\text{Ephoton1} - \text{Ephoton2}|}{\text{Ephoton1} + \text{Ephoton2}}$. Because the combinatoric background varies strongly with centrality and $\pi^0$ energy, a fixed asymmetry cut is not optimal for simultaneously rejecting background and maximizing statistics. We apply an asymmetry< 0.4+0.4*centc/100 cut for all $p_T$ >5GeV, where "centc" is the centrality.

In the high-$p_T$ region of interests, the pair of photons decay from $\pi^0$ are most likely to fly into the same EMCal sector. So we require that both photons be used in $\pi^0$ reconstruction must come from same EMCal arms. The purpose is to select good $\pi^0$ for our jet-tagging triggers, while not losing too much signal.

The cuts for $\pi 0$ are listed here:

$|\pi^0_{\mathrm{mass}} - 0.14| < 0.02$ GeV,

asymmetry < 0.4+centc*0.4/100,

both photons come from the same EMCal sector.

In the following plots, we showed the cut effects on pi0 invariant mass S/B ratio. The starting cuts for each plots is asymmetry <0.8 plus pi0's transverse momentum $p_T$ larger than 5 GeV. For the pi0invmass_assym_cent1 means, we add a cut asymmetry<0.4+0.004*centc. lemcpc3dz and lemcpc3dp are for the matching between PC3 projection and EMCal cluster. A close matching possibly means this EMCal cluster is from a charged hadron, and should be removed. For charge veto cut, we add a cut requiring $(\frac{\mathrm{lemcpc3dz}}{10})^2 + (\frac{\mathrm{lemcpc3dp}}{0.02})^2 > 1$, otherwise it's quite likely that the particle is high momentum charged hadrons. For the pi0invmass_all_cent1, it's the plot combining all the cuts of asymmetry and veto. All the invariant mass plots are under 0-10% centrality, because here has most background. The S/B ratio is significantly improved after applying the background cut. The sharper the shape is, the larger S/B ratio is. We fit the pi0 mass spectrum with a Gaussian function plus a third order polynomial. The Gaussian function stands for signals, and the binomial function stands for the background. We integral the x axis from 0.12 GeV to 0.16 GeV to get the magnitude of signal and background, therefore get the ratio. We only use the plots for most centrality (0-10%), it's because for the head-on

collisions, we have the most binary collisions and the most background, S/B ratio is lower than other centrality collisions.

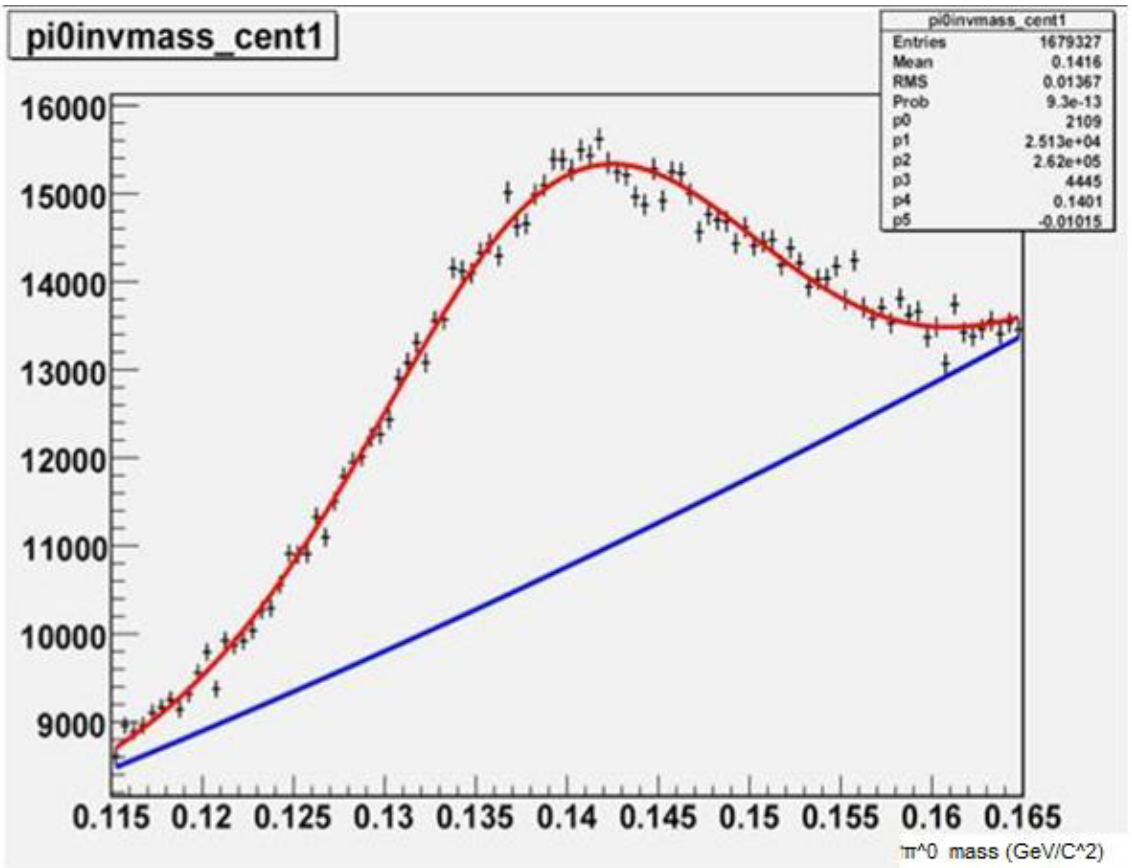


Fig.3. 15 pi0 invariant mass with starting cuts (asymmetry<0.8, lpt>5 GeV). The S/B ratio is 0.2. $[0] + [1] \times x + [2] \times x^2 + [3]\exp\left(\frac{x-[4]}{[5]}\right)^2$ ,[n] is fitting parameters.

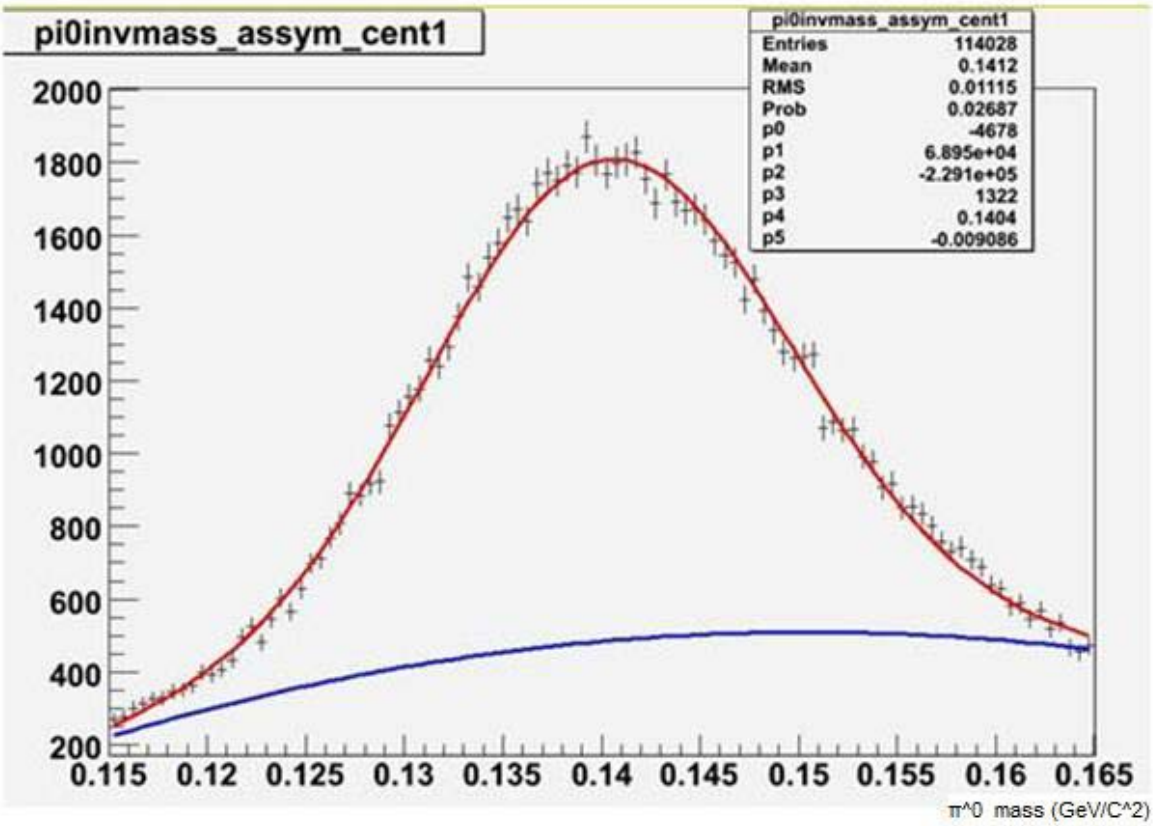


Fig.3.16 Pi0 invariant mass additionally with asymmetry cut: asymmetry< 0.4+0.004*centc.

The S/B ratio is 1.6. Fitting parameters as shown in the plot is the same meaning as last one.

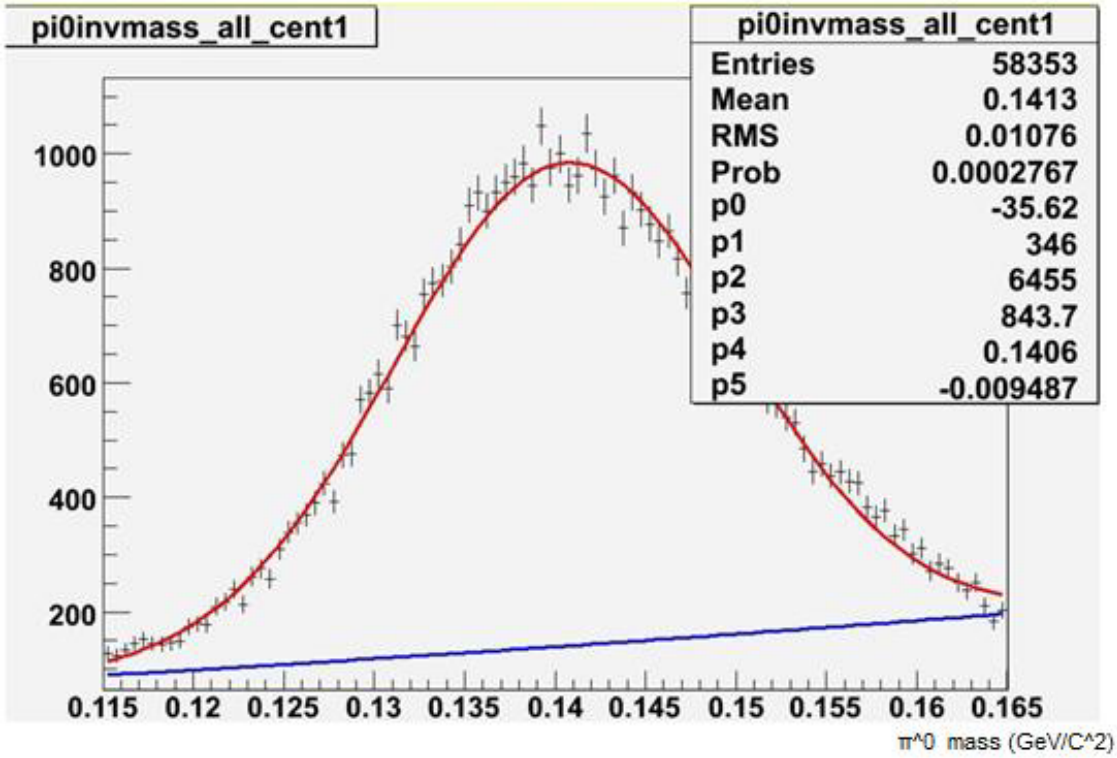


Fig. 3.17 plot of $\pi^0$ invariant mass with all promising cuts. The area under blue line is for the fitting background, the area between the red line and blue line is for the signal.S/B ratio is 3.5. The fitting parameters are the same as Fig.3.15 .

# CHAPTER 4. CORRELATION FUNCTION AND ZYAM METHOD

## 4.1 Construction of Correlation Function

Experimentally, the correlation is defined as

$$C(\Delta\phi, \Delta\eta) = \frac{\frac{dN_{pair}^{real}}{d\phi d\eta}}{\frac{dN_{pair}^{mix}}{d\phi d\eta}} \quad (4.1)$$

The numerator of Eqn. (4.1) is the raw joint pair distribution we get in the detector and we think it's the "real" event that we are studying. The denominator is the raw mixed pair distribution to represent the acceptance effect, which does not contain physical correlations. In this way, construction of the correlation function removes the pair acceptance from the "real" event distribution. The mixed pair distribution selected the pair particles from different events. Same pair-cuts are applied to real and mixed correlation to remove possible fragmented or split "ghost" tracks, if pairs are from the same category. Then the correlation function is proportional to the real pair distribution [22].

$$C(\Delta\phi, \Delta\eta) \sim \frac{dN_{pair}^{real}}{d\phi d\eta} \qquad (4.2)$$

In correlation function, each of both particles of a pair is within a range of momentum. Combination of ranges is arbitrary because the pair distribution is symmetric with respect to the particles. If both trigger and associated particle have the same transverse momentum range, it's called Fixed Correlation. Otherwise, it's called Assorted Correlation,

usually the trigger particle is in the highest momentum range and associated particle is in a lower momentum range.

Event will be further divided with respect to centrality and collision z-vertex bins. The real pair distribution in the bin is filled with all available pairs of particles in that event, which is the numerator in Eqn. (4.1). Number of triggers in this bin is recorded for later normalization [23]. In this way, we look for the statistical correlation of the particles produced by jets rather than reconstruct jets directly.

### 4.1.1 Event Mixing

The mixed event distribution is for removing physical sources of correlation so that the only source of the mixing distribution is the pair acceptance and efficiency. It can then be used to correct real event foreground correlation function. Since we are analyzing per-trigger yield, we don't need to correct single trigger efficiency here.

The technique that is employed is known as the "rolling-buffer" technique. A set of N trigger events which contains at least one trigger pi0 plus a conditional hadron, are kept in a "trigger-event" buffer. A set of general events sample, without trigger and/or conditional particle requirement, are kept in an "associated-event" buffer. Each time one trigger event enters the bottom of buffer, this trigger correlate with all "similar" (e.g. similar centrality and collision z-vertex) events from the associated buffer. When either buffer is full, the earliest event is removed from the buffer, and buffers are shifted for next event. This method is so called "rolling buffer" and it has variations.

In Au-Au, all events are divided into 3 centrality bins: 0-20%, 20-40%, 40-92%. 6 z-vertex bins between -30 to 30cm, 10cm each. Events only mix within same centrality and collision z-vertex bin. The rolling buffer method also ensures mixing events are within

closing time frame. We use a pure minimum bias sample of associated particles to avoid the space bias. A minimum bias event is selected by detector components other than the central arms. Here, we use BBC detector, which located at 3.1< η <4.0, as our minbias event selector. On the other hand, if trigger events and associated events are from two different set of detectors, that might produce "time bias", since they can be from different time periods and detected by different detector geometries.

### 4.1.2 Normalization

The correct normalization of the correlation function is necessary in order to extract the correct yield of pairs. A common way at RHIC is to report per trigger yields, where the correlation function is divided by the number of triggers and an appropriate normalization Ɲ is used. This normalization Ɲ satisfies (where the subscript "pair" from is dropped now on)

$$\frac{dN^{pair}}{N_{trig}d\phi d\eta} = Ɲ C(\Delta\phi, \Delta\eta) \quad (4.3)$$

The normalization constant can be derived [25] after η integration.

$$\frac{dN^{pair}}{N_{trig}d\phi} = \int Ɲ C(\Delta\phi, \Delta\eta)\, d\eta \quad (4.4)$$

### 4.1.3 $v_2$

Due to the elliptic flow, the azimuthal correlation of two particles can be expanded as

$$\frac{dN}{d\Delta\phi} = \int_0^{2\pi} d\phi_A \int_0^{2\pi} d\phi_B \frac{dN_A}{d\phi_A}\frac{dN_B}{d\phi_B}\delta\left(\Delta\phi - \phi_A - \phi_B\right) = \frac{N_A}{2\pi}\frac{N_B}{2\pi}\left(1 + 2v_2^A v_2^B \cos\left(2\Delta\phi\right)\right) \quad (4.5)$$

$v_2$ depends on transverse momentum. This shape will peak at both $\Delta\phi = 0$ and $\pi$, a feature similar to the jet and di-jet correlations discussed later. Fig.4.1 is a typical plot of pair distribution. The flow $v_2$ in Au-Au we applied here came from [24] . The $v_2$ for trigger and associated particles can be interpolating by the results as a function of transverse momentum and centrality in Fig 4.2.

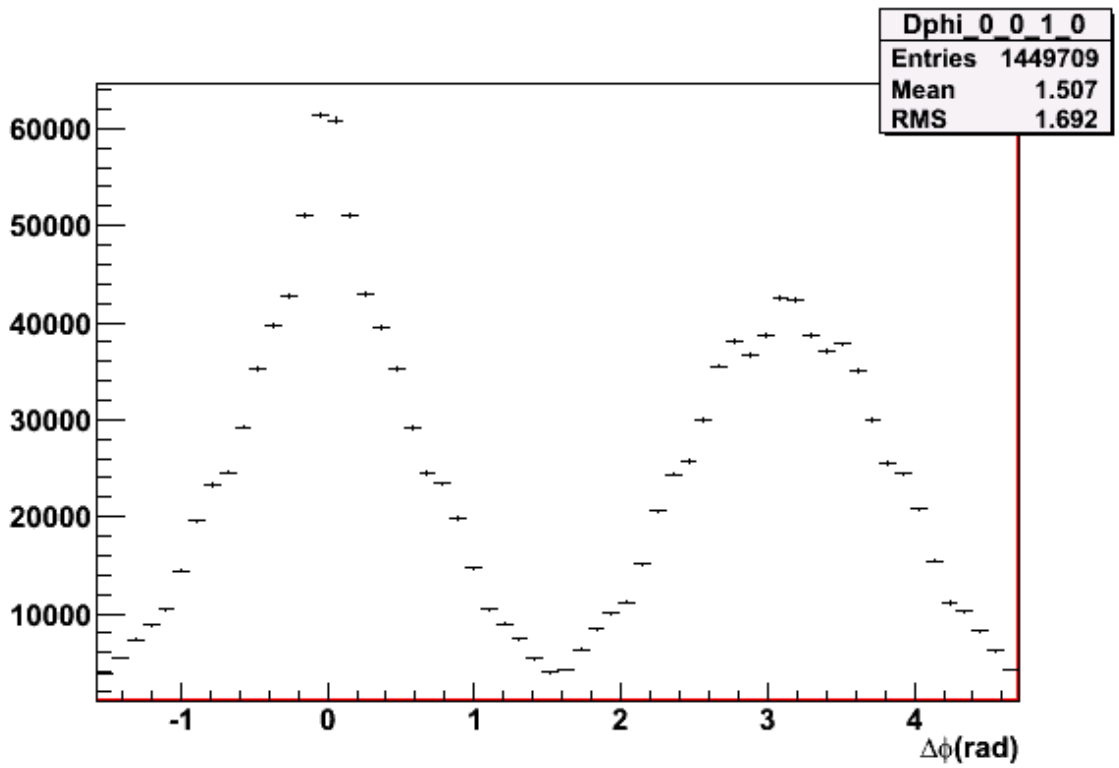


Fig.4.1 Raw Pair distribution of real events. It peaks at $\Delta\phi = 0$ or $\pi$.

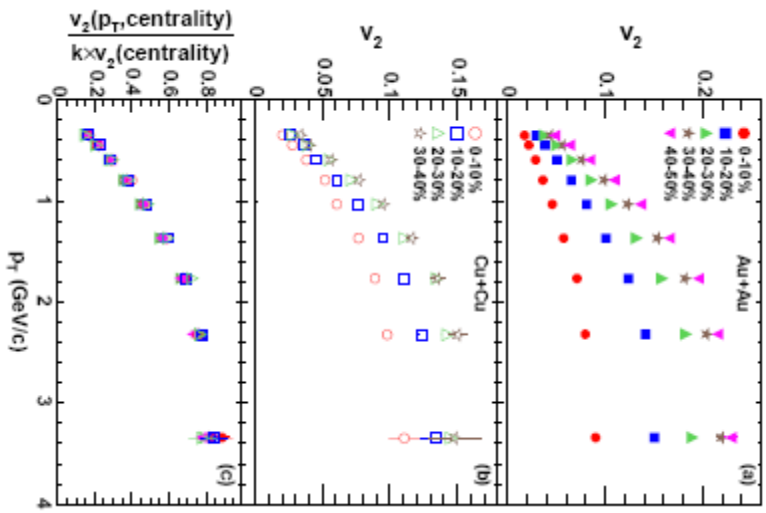


Fig.4.2 The published PHENIX measurement of $v_2$ in Au-Au and Cu-Cu as a function of centrality and $p_T$.

Our correlation function will be written into two items, the jets with the accompanying underlying event

$$\frac{dN^{pair}}{N_{trig}d\phi} = B\left(1 + v_2^{trig} v_2^{asso} \cos(\Delta\phi)\right) + J(\Delta\phi) \quad (4.6)$$

B is the underlying isotropic background, $v_2^{trig}$ and $v_2^{asso}$ are the trigger and associated particle's elliptical flow, and J ($\Delta\phi$) is the shape of the jet plus di-jet distribution. The jet function is derived as [25]

$$J(\Delta\phi) = \frac{S_N}{\sqrt{2\pi}\sigma_N} e^{\frac{-\Delta\phi^2}{2\sigma_N^2}} + \frac{S_F}{\sqrt{2\pi}\sigma_F} e^{\frac{-(\Delta\phi-\pi)^2}{2\sigma_F^2}} \quad (4.7)$$

N indicates near side, F indicates far side, which means in the back hemisphere of trigger particle. Jet function is sum of two Gaussian functions peaking at $\Delta\phi = 0$ and $\pi$. In

order to make the correlation function, we need to subtract the flow background from the raw per trigger yield.

## 4.2 ZYAM

ZYAM is a method short for stands for Zero-Yield-At-Minimum [26]. It means to shift the background so that the jet function has a minimum yield of zero. Firstly, the raw correlation function is corrected by acceptance and single particle efficiency, then we shift $\nu_2$ flow background curve from below, let it touch the raw correlation function, then, subtract the flow contribution from the raw correlation function to derive the jet shape or yield. We assume that both near and away-side jet yield, have a localized shape and won't affect other peak. Hence, there will be a small region where flow background dominates, and we make this region as a single bin in the correlation shape. In practice, we can employ the ZYAM method by fitting the raw function by a basic shape, which is a Gaussian plus a constant (flat background) at near-side, then, make the flow shape touch this fitting shape.

An example is shown in Fig.4.3, for the Cu-Cu correlation functions, with the trigger at $5 < p_T < 10$GeV/c, and associated charged tracks at $p_T$ = 1-2, 2-3GeV/c. All yields under the flow line is defined as flow background of underlying events, and the area between the flow and total line will be considered as our jet contribution.

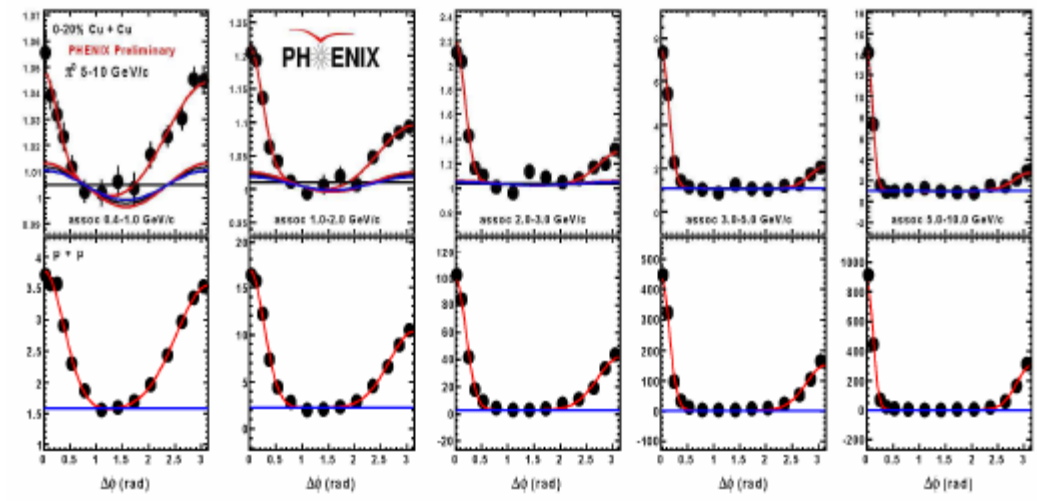


Fig.4.3 Comparing correlation functions of Cu-Cu (top) to p-p (bottom). Acceptance effects already corrected. Flow background from ZYAM method is marked on Cu-Cu plots.

## CHAPTER.5 Au-Au CORRELATION FUNCTION

From data analysis in chapter 3, the data for charged hadrons after applying multiple cuts, has a good signal to background ratio, with respect to 2 sigma and 1 sigma matching in PC3. The data analysis for trigger particle-$\pi^0$, has a high value of ratio of signal to background, with respect to pi0 invariant mass spectrum. These two conditions confirm the validity of our results in correlation function. Before we applied those quality cuts on data, the data is highly contaminated and can't be use to get a valid physics results. Any conclusions from highly contaminated data can be misguided, and can't be correct. Unless we have qualified data, also combined with systematic error corrections, reliable physics results or conclusion can be made. Fig. 5.1 shows a draft correlation function subjected to data analysis in former chapters with 0~10% centrality, $\pi^0$ $p_T$ > 5 Gev, associated charged hadron's $p_T$ is from 1 to 2 GeV. In this plot, it has a suppression on away-side of trigger

particle. This is not a "correct" result with only particle selections. For example, we also need to look at the acceptance cut for the next step, which can provide information of data's stability, plus further detail need to be considered for yield correction around $\Delta\phi \sim \pi$, the systematic errors, calculation of $\nu_2$ for ZYAM etc. Since we are doning a "2+1" correlation, the near side jets also travel certain distance in the hot dense matter, and with gluon radiation, we can expect a broader shape and suppression on the near side correlation function. Works will be done by a Ph.D study.

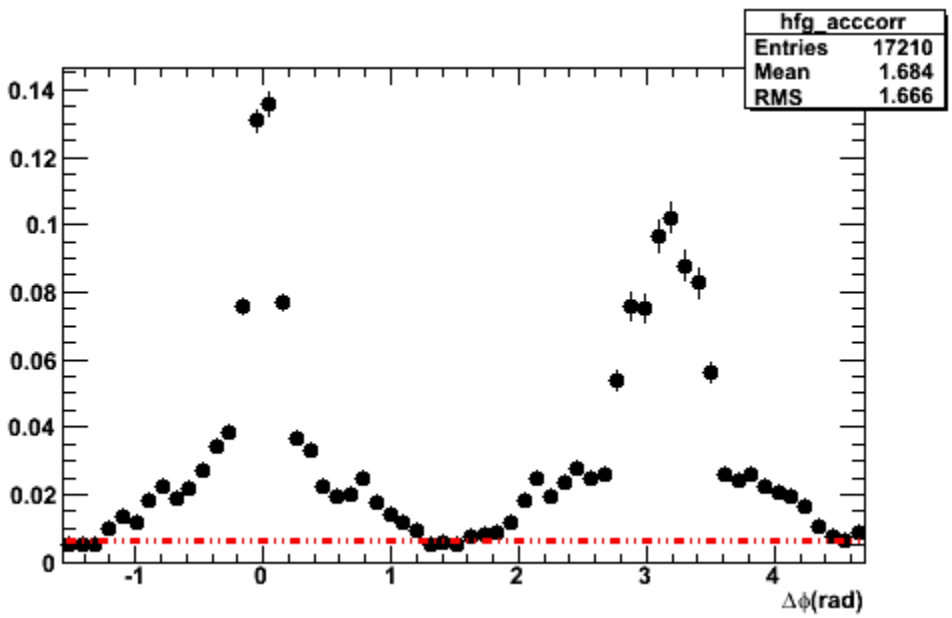


Fig.5.1Draft correlation function. The red line is straight line showing y=0 baseline.

# REFRENCES

[1] “Formation of dense partonic matter in relativistic nucleus-nucleus collisions at RHIC: Experimental evaluation by the PHENIX Collaboration” PHENIX QGP white paper, Nuclear Physics A Volume 757, Issues 1-2 , 8 August 2005, Pages 184-283, 2005-05-24.

[2] J D Bjorken. Highly Relativistic Nucleus-Nucleus Collisions: The Central Rapidity Region. Phys. Rev., D27:140, 1983.

[3] S. S. Adler et al. Systematic studies of the centrality and $\sqrt{s_{NN}}$ dependence of the dET /dη and dNch/dη in heavy ion collisions at midrapidity.
Phys. Rev., C71:034908, 2005, nucl-ex/0409015.

[4] S Catani et al. New Clustering Algorithm for Multi-Jet Cross Sections in e+ + e− Annihilation. Phys. Lett., B269:432–438, 1991.

[5] “Jet Properties from Di-Hadron Correlations in p+p Collisions at $\sqrt{s_{NN}}$ = 200 GeV”. Phys. Rev. D 74, 072002 (2006), 2006-10-05.

[6] Dihadron azimuthal correlations in Au+Au collisions at $\sqrt{s_{NN}}$ = 200 GeVarXiv:0801.4545

[7] V. Greco et al., Phys. Rev. Lett. 90, 202302 (2003) and Phys. Rev. C68, 034904 (2003).

[8] R. C. Hwa and C.B. Yang, Phys. Rev. C70 024905 (2004), and J. Phys G30 (2004) S1117-S1120.

[9] R. Fries et al., nucl-th/0407102 (2004).

[10] A. Majumder, E. Wang, X. N. Wang, nucl-th/0412061 (2004).

[11] N. Armesto, C. Salgado, U. A. Wiedemann, Phys. Rev. Lett. 93 242301 (2004)

[12] J. Casalderrey-Solana, E. V. Shuryak, D. Teaney, hep-ph/0411315 (2004)

[13] H St¨ocker, Nucl. Phys. A750 121 (2005)

[14]J. Ruppert and B. Muller, hep-ph/0503158 (2005)

[15] "Azimuthal Correlation and Conditional yield measurement at $\sqrt{s_{NN}}$ =200Ge in Au+Au, d+Au,p+p Collisions at RHIC. Anne Marie Sickles.

[16] PHENIX Conceptional Design Report. Unpublished.

[17] M. Allen et al. PHENIX Inner Detectors. NIM, A499:549–559, 2003.

[18] C. Adler et al. The RHIC Zero-Degree Calorimeters. NIM, A499:433–436, 2003.

[19] K. Adcox et al. PHENIX Central Arm Tracking Detectors. NIM,A499:489–507, 2003.

[20] High-*pT* Charged Hadron Suppression in *Au-Au* Collisions at $\sqrt{s_{NN}}$ = 200 GeV. Jiangyong Jia

[21] The complete volume Edited by M. Harrison, T. Ludlam and S. Ozaki, Volume 499, Issues 2-3, Pages 235-880 (1 March 2003) The Relativistic Heavy Ion Collider Project: RHIC and its Detectors.

[22] Jia, J. J. Phys. G31 (2005) S521-S532.

[23] Adams, J. et al. (STAR collaboration) nucl-ex/0411003

[24] PHENIX Collaboration, A. Adare et al. nucl-ex/0608033, Scaling properties of azimuthal anisotropy in Au+Au and Cu+Cu collisions at $\sqrt{s_{NN}}$ = 200 GeV/c

[25] Della Negra, M. et al. (CCHK collaboration) Nucl. Phys. B127 (1977) 1

[26] S. S. Adler et al. Phys. Rev. Lett. 97, 052301 (2006)